Title
On the Rupture Path of the 2019 Ridgecrest Earthquake Sequence

Permalink
https://escholarship.org/uc/item/9845w51h

Author
Cortez, Jordan

Publication Date
2022

Peer reviewed|Thesis/dissertation

UNIVERSITY OF CALIFORNIA
RIVERSIDE

On the Rupture Path of the 2019 Ridgecrest Earthquake Sequence

A Thesis submitted in partial satisfaction
of the requirements for the degree of

Master of Science

in

Earth and Planetary Sciences

by

Jordan Cortez

March 2023

Thesis Committee:
      Dr. David Oglesby, Chairperson
      Dr. Roby Douilly
      Dr. Abhijit Ghosh

The Thesis of Jordan Cortez is approved:

_____

_____

_____
                                                    Committee Chairperson

University of California, Riverside

Table of Contents

List of Figures

Chapter 3

1. A synopsis of the 2019 Ridgecrest earthquake sequence

The 2019 Ridgecrest earthquake sequence (RES) was a remarkable event in a number of ways. It consisted of two large earthquakes (the largest to hit Southern California in decades) and numerous small- to moderate-sized earthquakes on a complicated crisscross of nearly parallel and perpendicular fault segments, with branches and stepovers at multiple scales as shown in figure 1.2. The observational datasets of the RES are discussed in section 1.1; Overall, this behavior of the RES is likely related to the tectonic setting of the Southern Walker Lane, north of Garlock fault within the Eastern California Shear zone, which is shaded in gray in figure 1.1. The entire walker lane and eastern california shear zone accommodates ~20% of the strain due on the plate boundary between the North American and Pacific tectonic plates [Faulds and Henry, 2008]. Consequently, en echelon left-stepping dextral faults are observed in the region with an overall orientation parallel to the plate motion, analogous to Riedel shears [Faulds et al. 2005]. This dominated left stepping dextral conjugated orthogonal faulting pattern was also observed in the northern Walker Lane during the 2016 nine-mile earthquake sequence, located at the top of figure 1.1 north of mono lake, consisted of three Mw 5.4–5.6 earthquakes within one hour of each other near Fletcher Valley, Nevada (Hatch-Ibarra et al. 2022).
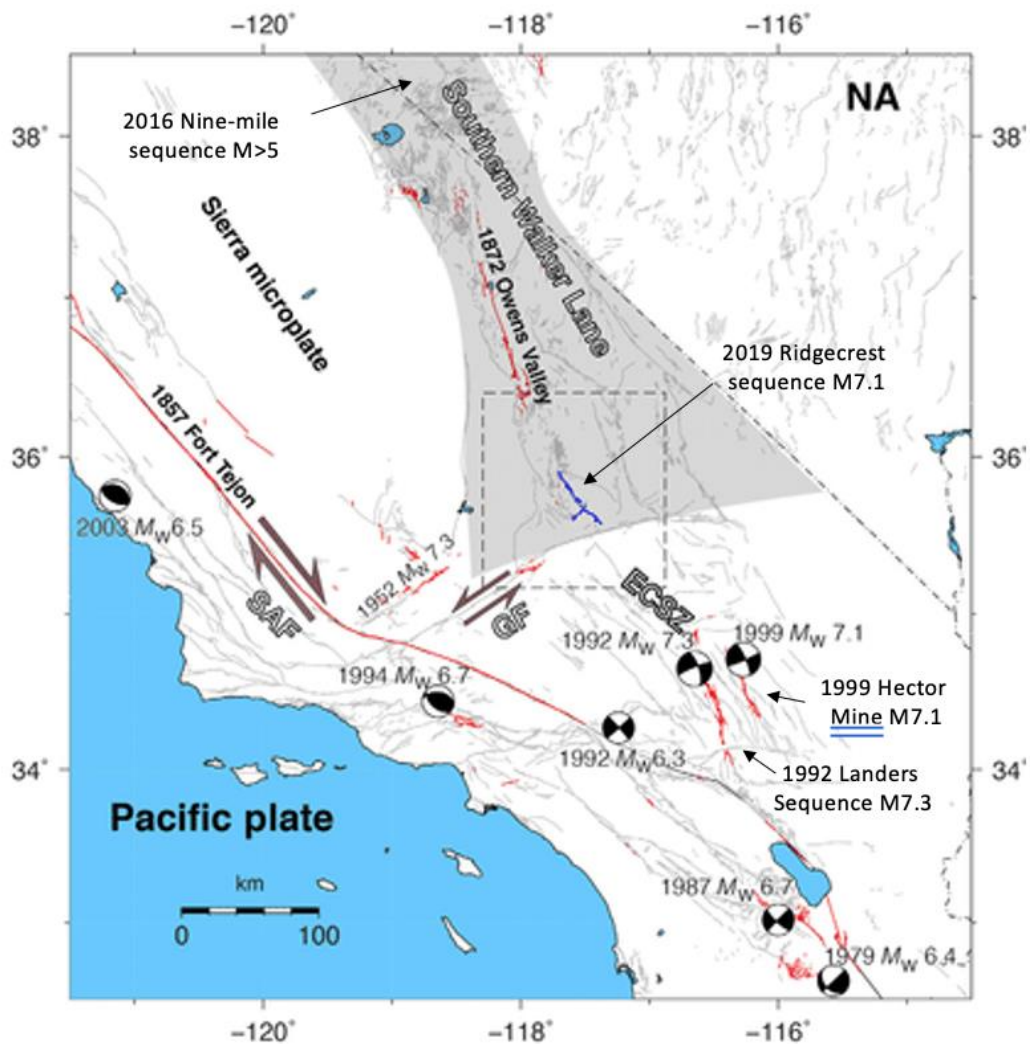
Figure 1.1 Illustrates the tectonic setting of the 2019 RES: focal mechanisms of historically large earthquakes and corresponding faults within Southern California and Nevada (Wang et al 2020). The San Andreas Fault (SAF) zone outlines the plate boundary between North American and Pacific plates, while the Garlock fault (GF) separates the Southern Walker lane (gray shaded zone) and Eastern California shear zone (ECSZ). The 2019 RES faults are outlined in blue, while the 1992 Landers and 1999 Hector mine earthquake sequences are outlined in red. The 2016 Nine mile earthquake sequence faults aren't shown but the location is shown north east of mono lake, near the California-Nevada border, rupturing in Nevada (NA).

2

Larger extended strike slip faulting without the orthogonal faulting pattern is observed within the eastern California shear zone. A couple of historically large earthquakes such as the 1992 Landers and 1999 Hector mine sequences resulted in approximately 100km and 48km of left stepping dextral slip, respectively (Hauksson et al 1993; Pollitz et al 2002). These M7+ earthquake sequences occurred within the Eastern California shear zone, south of the Garlock fault, outside the regional stress of the Owens valley, and faults are outlined in red in figure 1.1. The geological setting may explain the larger surface rupture to seismic moment ratio in this region compared to the RES area. In addition to the reduced slip to seismic moment ratio, the seismic moment of the M6.4 RES foreshock wasn't enough to immediately trigger the subsequent mainshock, even with its proximity and intersecting faults. It's also perhaps surprising that the smaller nine-mile M5+ earthquakes released stress in 1-hour intervals, compared to the 36-hour time interval between the M6.4 and M7.1 earthquakes during the RES. Another unique feature regarding the RES but not investigated in this thesis is the duration of the seismic attenuation and corresponding intensity at long distances. The high frequency waves traveled past the mountain range from Ridgecrest, California, leaving Southern California with slight shaking. The purpose of this thesis is to underline the effects of both self-induced stress interactions and fault interaction influences on the rupture propagation and overall slip distribution for conjugated strike slip faulting into the RES.

This section of Chapter 1 provides general information concerning the RES and its relation to Walker Lane. Sections 1.1-1.3 lays out the observational datasets, models used, and results of prior observational models, including rupture propagation and slip distribution. Chapter 2 focuses on the first large M6.4 earthquake of the RES, while Chapter 3 describes our numerical model for the M7.1 mainshock both with and without the effects of the prior M6.4 foreshock. Lastly, Chapter 4 summarizes my findings and interests regarding the RES.

1.1 Fundamental Observations of the RES

The ground displacement and fault offset due to this earthquake sequence have been measured using field observations, seismic data, and geodetic data (i.e InSAR, GPS, etc). Figure 1.2a displays the mapped surface fault geometry (Kendrick et al., 2019) of the earthquake sequence, as well as the aftershock distribution, indicating that the aftershocks do not necessarily line up perfectly with the apparent mapped surface faulting. The first event in this sequence, the M6.4 earthquake, took place primarily on a set of left-lateral faults striking to the NE. The left-lateral fault traces are defined by significant surface faulting evidence, but seismological, and geodetic models (e.g., Ross et al., 2019; Li et al., 2020; Pollitz et al., 2020), and aftershock studies (Lomax, 2020; Shelly, 2020) imply that the M6.4 rupture may have initiated on a buried right-lateral fault segment that intersects the left-lateral segments almost orthogonally, toward the NE edge of the left-lateral system (Figure 1.2a; blue-colored seismicity).

Around 30 hours later, an M 5.4 aftershock took place to the NW of the edge of the possible right-lateral segment of the M6.4 earthquake. Finally, 6 hours after the M5.4 event, an M7.1 earthquake nucleated a short distance to the west of the M5.4, and propagated on a SE-striking right-lateral system of faults that crossed the original M6.4 fault system and continued beyond to the SE for a number of km. It is notable that the M7.1 event did not appear to re-rupture the buried right-lateral segment that participated in the M6.4 quake, but rather took a more southwestern, almost-parallel branch to cross the left-lateral M6.4 fault (as indicated by distinct aftershock clouds—red versus blue in Figure 1.2a—from the two events). In addition to the geometry, the Kendrick et al (2019) field observations consist of direct measurements of deformation and slip. The ground displacements from a geodetic expedition (figure 1.2b) and strong ground motion from a seismic array (figure 1.2C) are consistent with the field expedition's direct measurements (kendrick et al 2019). Rekoske et al (2019) provides a robust ground motion dataset including 22,375 records from 131 events from 4 July 2019 to 18 October 2019 with a magnitude range from 3.6 to 7.1. Plesch et al 2020 provides a detailed interpretation of the RES fault geometry using a similar seismic array in the region. These datasets were used for inverse models of the RES, discussed in the next section.

1.2 Slip distribution using Inversion modeling

Inversion models utilize data gathered from geodetic and seismic instruments to infer slip models for an earthquake that can be compared to or augmented by direct field measurements. Essentially these models invert for measurables (i.e. slip, velocities, etc) using the changes in deformation detected from satellites & antennas, seismometers, etc. Figure 1.2 provides a spatial comparison of field-mapped surface traces (figure 1.2a), GPS stations (figure 1.2b) and Seismic stations (figure 1.2c) relative to the seismicity and ground displacement of the RES. Kendrick et al (2019) is one of a few RES field expeditions that determined direct slip measurements, measured ground displacements, and mapped surface ruptures (figure 1.2a). These observations are used to validate inverse studies by comparing their models' results derived from data gathered by their instrumentation. Chen et al (2019) compared GPS displacements from satellite imaging during the M7.1 mainshock with synthetics generated from a forward model and direct measurements as shown in figure 1.2b. Pitarka et al (2021) utilized the seismic stations and dataset provided by Rekoske et al (2019) to invert for the fault slip (figure 1.2c). Yu et al (2021) designed a similar linear inversion algorithm (based on Hartzell and Heaton, 1983) to simultaneously invert for the foreshock and mainshock space-time slip evolution using the same strong ground motion dataset, which is in strong agreement with the seismic spatial distribution in figure 1.2a. Hough et al (2020) also utilized Rekoske et al (2019)'s ground motion dataset (figure 1.2C) to determine the near-field shaking intensities at hard rock sites near the main shock hypocenter (station CLC) and soft sites

south of the mainshock surface ruptures (station CCC) to a nonlinear response of the sediments themselves. This result expresses how complex and nonlinear the relationship is between the geology of the rocks and response to seismic waves in terms of ground motion. The uncertainties in the ground displacement measurements introduce challenges for inversion modeling, including non-physical interpretations in their parameterization, temporal limitations for data collecting, and data filtration. These differences explain some of the ambiguity in characterizing the overall fault slip distribution and postseismic deformation produced by geodetic (figure 1.3) and seismic (figure 1.4) modeling. The basic consensus among the slip models produced by the different techniques is a bilateral rupture pattern with spatially variable slip, with slight disagreements in the locations of peak slip. Despite the ambiguity, the isolated slip produced by only the M6.4 foreshock using geodetic and seismic inversions agrees with the conjugated rupture pattern depicted by the surface traces in figure 1.2. The ambiguity in parameter space for inversion models lies with their lack of identifying the source of each feature. However, a forward dynamic model approach underlines the presence and effects of important physical mechanisms, allowing for a more intuitive source parameter analysis. Thus, correlating dynamic modeling with inverse measurables can produce more realistic results with physical interpretations (Ramos et al 2020). Ramos et al (2020) constructed a robust model comparison between inverse kinematic and forward dynamic modeling approaches as shown in figure 1.4C. Their dynamic model produced a slip distribution similar to the geodetic inversions in figure 1.3 excluding the regions near the hypocenter of the mainshock, where their dynamic model accounts for the dynamic stress drop effects.

1.3 Rupture propagation and slip distribution

An important feature in an earthquake's behavior is its rupture propagation, namely the path and speed the rupture takes as it propagates along the fault, allowing slip and the release of elastic energy. The finding that earthquakes radiate seismic waves because of releasing stored energy is an implication of elastic rebound theory, which describes the elastic and slip response of a fault embedded in an elastic solid. Rupture propagation on perpendicular faults such as in the Ridgecrest sequence has been the subject of several numerical studies in the past (e.g., Kase and Kuge, 1998; Magistrale and Day, 1999; Kase and Kuge, 2001, Lozos, 2022), and such work has been used to help explain rupture propagation in geometrically complex fault earthquakes such as the 2012 Sumatra Earthquake (Meng et al., 2012). In general, research has implied that it is likely easier for rupture to propagate around an extensional corner than a compressional corner. Kyriakopoulos et al. (2019) notes that the ability of rupture to propagate around a corner can be strongly sensitive to the details of rupture propagation due to the competing effects of dynamic clamping, unclamping, and shear stress changes.

In addition to the fault orientation in terms of normal traction direction, bends and turns within the fault geometry introduce traction heterogeneity due to both the regional stress field, in a static sense, and neighboring faults' coseismic slip interaction, in which both mechanisms have been shown to influence rupture propagation (Madden et al 2013; Mildon et al 2019; Oglesby et al 2003). This effect emphasizes the importance in including non-planar faulting characteristics; otherwise an artificial stress drop must be applied to account for this effect in an assumed planar fault geometry (Peyrat et al 2001; Pollitz et al 2019;). Other influences of rupture propagation include directivity and hypocenter location, related parameters that govern the path of seismic radiation and the fault's response relative to where the seismic energy is released. We explore such effects in this thesis regarding the rupture propagation and resulting slip distribution in consequence of the M6.4 foreshock and M7.1 mainshock during the RES.
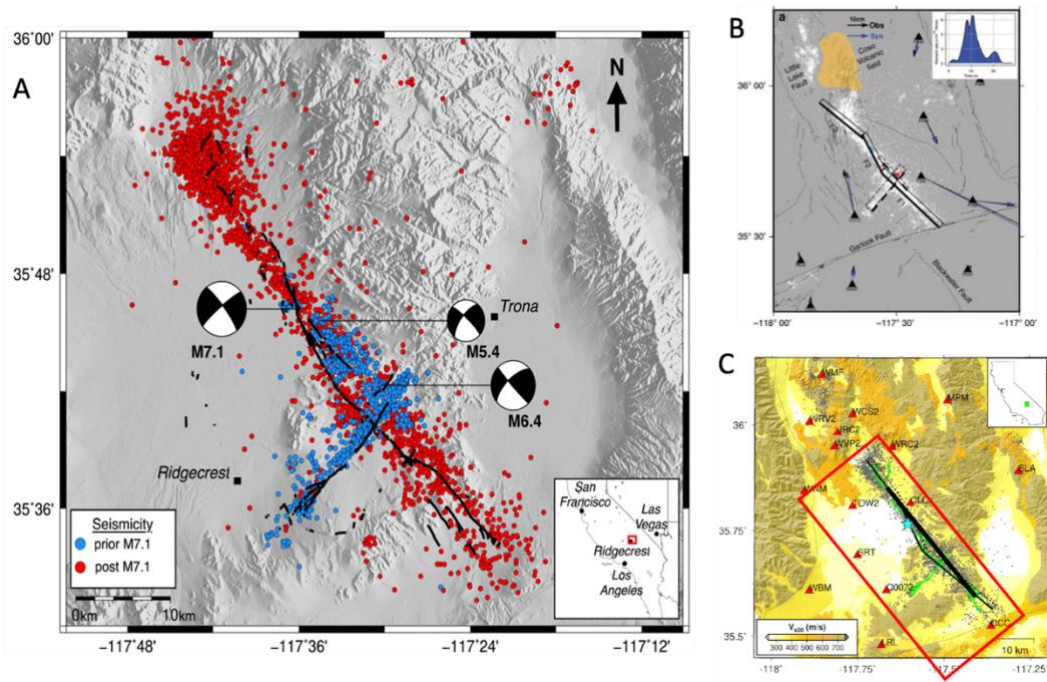
Figure 1.2A. Map view of our modeled fault geometry based on surface rupture and seismicity at depth. Mapped surface rupture (black curves), main earthquakes displayed by Focal mechanisms, and seismicity during the Ridgecrest sequence (white dots), and small seismicity color-coded by timing (blue: prior to M7.1 event; red: after M7.1 event). Figure 1.2B Co-seismic GPS from satellite imaging stations (black triangles) relative to synthetics constructed from a source model of the M7.1 event using planar fault geometry (black lines) (chen et al 2020). Figure 1.1C Spatial distributions of the seismic stations relative to the observed surface traces (black line) and empirical ground motion (green line) (Pitarka et al 2021).
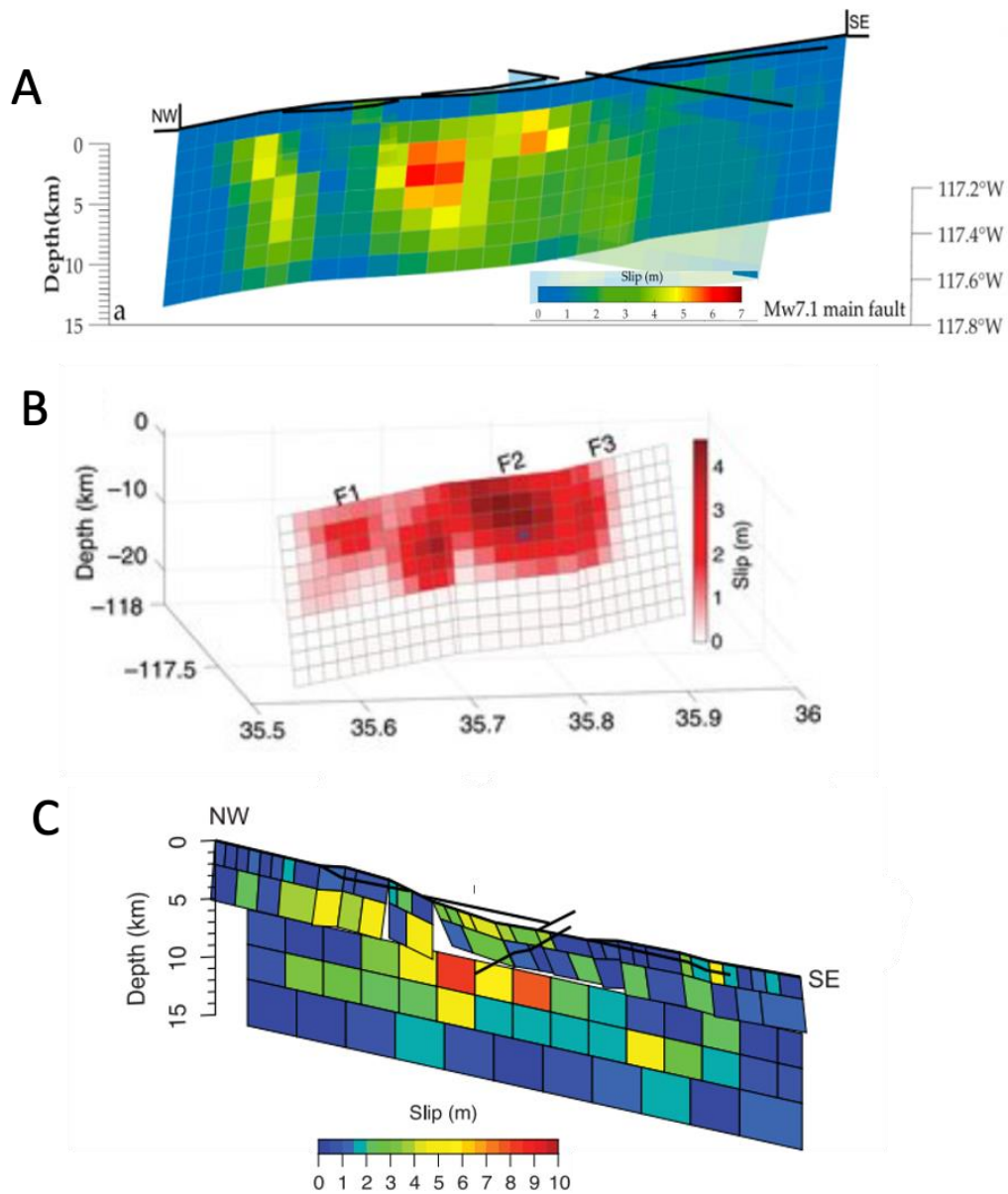
Figure 1.3A Slip distributions for the M7.1 event using optical images and InSAR displacement constraints (Li et al., 2020). Figure 1.2B Slip for the 3 subfault M7.1 mainshock depicted from an kinematic model using GPS measurements (Chen et al. 2020). Fig 1.3C Static slip inversion for the M7.1 mainshock using a damage proxy map and Coseismic interferogram derived from satellite InSAR coherence data (Ross et al 2019).
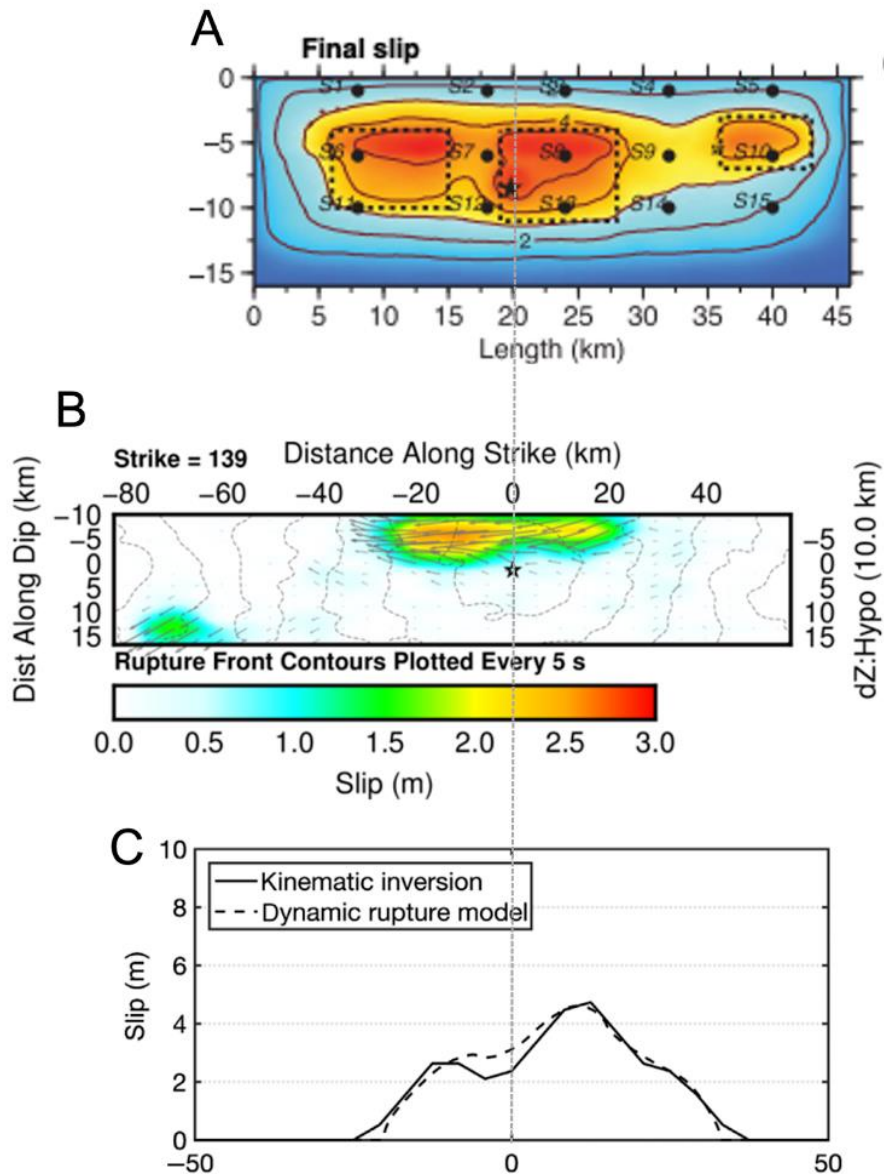
Figure 1.4 Comparison of slip models for the M7.1 mainshock event from 3 different studies. The hypocenter is represented in all 3 models by the gray dashed line. Figure 1.4A Slip distributions of the mainshock derived from a dynamic model using an inverted stress drop on planar fault geometry from strong ground motions. (Pitarka et al 2021) Figure 1.4b A slip distribution of the M7.1 mainshock event from the USGS database using seismic inversions of the M7.1 event with a finite fault inverse algorithm (Ji et al.,2002). Figure 1.4C A slip comparison between kinematic and dynamic models of the M7.1 mainshock, derived for an ideal optimization workflow (Ramos et al 2020).

References

Chen, K., Avouac, JP., Aati, S. et al. Cascading and pulse-like ruptures during the 2019 Ridgecrest earthquakes in the Eastern California Shear Zone. Nat Commun 11, 22 (2020). https://doi.org/10.1038/s41467-019-13750-w

Faulds, J.E., and Henry, C.D. (2008). Tectonic influences on the spatial and temporal evolution of the Walker Lane: An incipient transform fault along the evolving Pacific – North American plate boundary, in Spencer, J.E., and Titley, S.R., eds., Ores and orogenesis: Circum-Pacific tecton

Faulds, J.E., Henry, C.D., and Hinz, N.H. (2005). Kinematics of the northern Walker Lane: An incipient transform fault along the Pacific – North American plate boundary: Geology, v. 33, no. 6, p. 505-508.

Gabriel,A . Taufiqurrahman, .Carena,S. Ulrich, T. Li,D. Li,B. Wirp,A. Verdecchia,A. Gallovic,M. Gallovic,F. (2020). Untangling the dynamics of the 2019 Ridgecrest sequence by integrated dynamic rupture and Coulomb stress modeling across an immature 3D conjugate fault network. EGU. Presentation

Hough, S. E., E. Thompson, G. A. Parker, R. W. Graves, K. W. Hudnut, J. Patton, T. Dawson, T. Ladinsky, M. Oskin, K. Sirorattanakul, et al. (2020). Near-Field Ground Motions from the July 2019 Ridgecrest, California, Earthquake Sequence, Seismol. Res. Lett. 91, 1542–1555, doi: 10.1785/ 0220190279.

Hatch-Ibarra,R.L. Abercrombie,R. Ruh,C.J. Smith,K. Hammond,W, Pierce,I (2022). The 2016 Nine Mile Ranch Earthquakes: Hazard and Tectonic Implications of Orthogonal Conjugate Faulting in the Walker Lane. Bulletin of the Seismological Society of America (2022) 112 (3): 1727–174

Kendrick, K. J., S. O. Akciz, S. J. Angster, J.-P. Avouac, J. Bachhuber, S. E. Bennett, K. Blake, S. Bork, B. A. Brooks, P. Burgess et al. (2019). Geologic observations of surface fault rupture associated with the Ridgecrest M6.4 and M7.1 earthquake sequence by the Ridgecrest Rupture Mapping Group, in *2019 SCEC Annual Meeting*, Palm Springs, CA

Li, S., G. Chen, T. Tao, P. He, K. Ding, R. Zou, J. Li, and Q. Wang (2020). The 2019 Mw 6.4 and Mw 7.1 Ridgecrest earthquake sequence in Eastern California: rupture on a conjugate fault structure revealed by GPS and InSAR measurements, *Geophysical Journal International* **221,** 1651-1666.

Lomax, A. (2020). Absolute location of 2019 Ridgecrest seismicity reveals a shallow Mw 7.1 hypocenter, migrating and pulsing Mw 7.1 foreshocks, and duplex Mw 6.4 ruptures, *Bulletin of the Seismological Society of America* **XX**.

Lozos, J. C. (2022). Dynamic rupture modeling of coseismic interactions on orthogonal strike-slip faults. *Geophysical Research Letters*, *49*, e2021GL097585. https://doi.org/10.1029/2021GL097585

Madden, E. Maerten, F., and Pollard, D. D. (2013), Mechanics of nonplanar faults at extensional steps with application to the 1992 M 7.3 Landers, California, earthquake, J. Geophys. Res. Solid Earth, 118, 3249– 3263, doi:10.1002/jgrb.50237.

Mildon, ZK. Roberts, GP. Walker, JP. Toda,S (2019). Coulomb pre-stress and fault bends are ignored yet vital factors for earthquake triggering and hazard. Nat Commun. 2019 Jun 21;10(1):2744. doi: 10.1038/s41467-019-10520-6. PMID: 31227694; PMCID: PMC6588554

Oglesby, D and Archuleta, R (2003). The Three-Dimensional Dynamics of a Nonplanar Thrust Fault. Bulletin of the Seismological Society of America, Vol. 93, No. 5, pp. 2222– 2235, October 2003

Peyrat, S., Olsen, K. B., & Madariaga, R. (2001). Dynamic modeling of the 1992 Landers earthquake. *Journal of Geophysical Research*, 106(B11), 26467-26482.

Plesch, A. John, S. Ross, Z. Hauksson, E.(2020) Detailed 3D Fault Representations for the 2019 Ridgecrest, California, Earthquake Sequence. *Bulletin of the Seismological Society of America* 2020; 110 (4): 1818–1831. doi: https://doi.org/10.1785/0120200053

Pollitz, F. F., J. R. Murray, J. L. Svarc, C. Wicks, E. Roeloffs, S. E. Minson, K. Scharer, K. Kendrick, K. W. Hudnut, and J. Nevitt (2020). Kinematics of Fault Slip Associated with the 4–6 July 2019 Ridgecrest, California, Earthquake Sequence, *Bulletin of the Seismological Society of America*.

Rekoske, J., E. M. Thompson, M. P. Moschetti, M. Hearne, B. T. Aagaard, and G. A. Parker (2020). The 2019 Ridgecrest, California, Earthquake Sequence Ground Motions: Processed Records and Derived Intensity Metrics, Seismological Research Letters. 91 (4): 2010–2023. doi: https://doi.org/10.1785/0220190292

Ross, Z. E., B. Idini, Z. Jia, O. L. Stephenson, M. Zhong, X. Wang, Z. Zhan, M. Simons, E. Fielding, S.-H. Yun et al. (2019). Hierarchical interlocked orthogonal faulting in the 2019 Ridgecrest earthquake sequence, *Science* **366,** 346-351.

Stephen H. Hartzell, Thomas H. Heaton; Inversion of strong ground motion and teleseismic waveform data for the fault rupture history of the 1979 Imperial Valley, California, earthquake. Bulletin of the Seismological Society of America 1983;; 73 (6A): 1553–1583. doi: https://doi.org/10.1785/BSSA07306A1553

Shelly, D. R. (2020). A high-resolution seismic catalog for the initial 2019 Ridgecrest earthquake sequence: foreshocks, aftershocks, and faulting complexity, *Seismological Research Letters* **XX**.

Yue,H. Sun, J. Wang, M. Shen, Z. Li,M. Xue,L. Lu,W. Zhou,Y. Ren,C. Lay,T (2021). The 2019 Ridgecrest, California earthquake sequence: Evolution of seismic and aseismic slip on an orthogonal fault system

Wang, K. Dreger, D. Tinti, E. Burgmann, R. Taira, T. (2020). Rupture Process of the 2019 Ridgecrest, California Mw 6.4 Foreshock and Mw 7.1 Earthquake Constrained by Seismic and Geodetic Data. Bulletin of the Seismological Society of America. 110. 10.1785/0120200108.

2.1 The M6.4 foreshock

The M6.4 Searles Valley earthquake occurred on July 4th, 2019, and served as a foreshock of the M7.1 Ridgecrest earthquake, which occurred 30 hours later on July 5th. The observationally-inferred rupture path in the M6.4 demonstrates conjugate strike-slip faulting, represented by the seismicity in blue in figure 1.2a. The spatial and temporal distribution in Shelly's (2020) seismic catalog suggest that the M6.4 initially ruptured along a buried right lateral fault toward the Southwest until rounding an orthogonal corner to continue on a left lateral fault. The rupture then crossed over the fault of the subsequent mainshock with no field evidence of rupture on the right lateral mainshock fault. Complementing seismic data, Geodetic studies provide prior, coseismic, and post ground deformation observations, underlying mechanisms including afterslip and viscous relaxation, depending on the apparatus limitations such as temporal placement of antennas for GPS expeditions or the time interval of the satellite orbits for InSAR studies. Funning et al. (2020) gathered sequential GPS data between the foreshock and mainshock, thus allowing the identification of the ground displacement due solely to the M6.4 foreshock. These data provided evidence of re-rupture on the M6.4 left-lateral fault during the M7.1 mainshock.

Using cosesimic GPS constraints, Funning et al (2020) modeled the M6.4 foreshock and M7.1 mainshock independently, concluding that both events result in slip near the M7.1 hypocenter on the mainshock fault, and on the Northeast area of the M6.4 fault, across the fault intersection. However, the consequent deformation from the individual events are difficult to distinguish from InSAR datasets (figure 1.2).

In this chapter, we use 3D dynamic rupture modeling to investigate how and why the rupture process of the M6.4 earthquake allowed slip on two orthogonal fault segments, but did not coseismically trigger slip on the overlapping and intersecting M7.1 earthquake fault system. We do not attempt to model heterogeneous slip patterns or precise rupture timing. Our approach contrasts with that of Lozos and Harris (2020) and Taufiqurrahman et al. (2019), who modeled the entire Ridgecrest sequence with an emphasis on producing generally realistic fault slip patterns. In the present work, we take a detailed look at the time evolution of the M6.4 event and its stress interaction with the M7.1 fault system. A key result is that the burial depth of the right-lateral fault in the M6.4 event may have had a crucial role in determining the behavior of the entire fault system. We also find that only a narrow range of fault stress amplitude and a small subset of potential nucleation locations result in the observed rupture path of the M6.4 event. The results have implications for our understanding of this earthquake sequence's foreshock behavior, as well as for fault mechanics in general.

2.2 Method

2.2.1 Geometry

Although our goal is to model only the M6.4 Ridgecrest earthquake in this chapter, our modeled fault system includes the mapped and inferred fault structures for both the M6.4 and M7.1 events. The fault geometry was constructed using a combination of mapped surface rupture (Kendrick *et al.*, 2019) and seismic aftershock data obtained by template matching and precise relative relocation techniques (Shelly, 2020), which together typically serve as primary indicators for the location and extent of a causative fault for an earthquake. Most of the 3D representation of the fault system is obtained by projecting the mapped surface rupture vertically into the Earth for 15 km. However, some aftershocks of the M6.4 event appear to be on a surface roughly parallel to but NE of the main M7.1 event (Figure 1.2A), indicating the participation in the early event of an additional right-lateral fault segment with no surface expression. This buried segment serves as the location of the M6.4 hypocenter and likely intersects the main surface-rupturing M6.4 fault (Ross *et al.*, 2019). We fit a vertical plane to these aftershocks to produce a buried fault segment as part of our larger 4-segment fault system.

2.2.2 Mesh

We implement our fault model in a 3D finite element mesh via TRELIS software. The mesh consists of 4 million hexahedral elements with edge lengths of 200 m near the rupture area with an approximate fault system width of 16km and 600 m in the outer region. More specifically the fault segments implemented in our model lie within a volume with a higher density of element. Figure 2.1 illustrates the 2D fault traces and the 3D fault geometry in the context of our results for nucleation location (to be discussed later). For simplicity, and to isolate the effects of fault geometry on the earthquake rupture path and extent, we embed our fault in a homogeneous half space with wavespeeds VP=5477 m/s and VS=3162 m/s and density ρ=2700 kg/m3 (Barall, 2009). We note that most finite element methods require that a node at a fault intersection may slip in only a single direction associated with one of the segments at the intersection; thus, depending which way one assigns the slip direction to the node at the intersection, one fault is effectively continuous and "cuts" the other (discontinuous) fault.

We choose segment 1 (M6.4 right-lateral hypocentral fault) to cut segments 2 (M6.4 left-lateral surface rupture) and 3(left-lateral spur), and segment 2 to cut segment 4 (M7.1 mainshock fault) as illustrated in the fault geometry schematic in Figure2.1. Research on branched faults (DeDontney *et al.*, 2012; Douilly *et al.*, 2020) has indicated that rupture is slightly favored on the continuous fault. Thus, our choice of continuity in our fault mesh means that we may be slightly biasing the results away from propagation around the corners at the segment intersections.

2.2.3 Dynamic modeling

We carry out 3D dynamic rupture models using the code FaultMod (Barall, 2009), which has been utilized and extensively verified with other fault dynamics codes (Harris *et al.*, 2009; Harris *et al.*, 2011). We utilize a slip weakening friction law (Palmer and Rice, 1973; Andrews, 1976) with a static friction s=0.6, sliding friction s=0.1, and a slip weakening parameter 0.12 m. This relatively low weakening distance allowed us to generate nucleate rupture on the small M6.4 hypocenteral fault without needing a large artificial stress drop. Nucleation was accomplished by reducing the static friction coefficient to a failure level of 0.9 times the ratio of the shear to normal stress in an expanding circle (maximum radius 5000 m) on the fault surface at a forced velocity of 2000 m/s.

For simplicity we primarily use a constant traction pre-stress over the fault system to model the poorly constrained stress field; the shear stress is tuned to produce a realistic average fault slip in the M6.4 event of approximately 1 m (Ross *et al.*, 2019), although we note that we do not attempt to match the observed or inferred slip in any detailed sense. The normal stress is 6 MPA, and we test shear stresses of 2.1 MPa, 2.3 MPa, 2.4 MPa, and 2.5 MPa. To determine the sensitivity of the results to the near-surface stress condition, in some models we decrease linearly the shear and normal stresses from their ambient value at a depth of 1 km to one tenth of their ambient value at the free surface. By direct inspection we find that models have at least 4 elements in the breakdown zone at all times, corresponding to an adequate resolution of the slip weakening process. Besides stress, key variables we test in our models are the depth of burial of the right-lateral nucleating fault segment, which has an impact on the stress transfer to nearby segments, and the nucleation location, which affects the sequential order and amplitude of clamping/unclamping and increased/decreased shear stress between different fault segments.

2.3 Results

2.3.1 Effect of nucleation location along strike

The hypocenter location for the M6.4 event is reasonably well constrained (Ross *et al.*, 2019; Shelly, 2020). However, it is still useful to run models with different hypocenter locations to shed light on how likely the observed rupture path was (i.e., whether the results depended crucially on the hypocenter location). More importantly, such models can illustrate the effects of the time-dependent stress transfer between the fault segments as the rupture propagates through the system. Figure 2 shows 5 different hypocenter locations (A through E) and their resultant slip distributions using the shear stress and nucleating fault burial depth from our preferred model above. A key result is that only hypocenters located on the buried right-lateral segment 1, and that are relatively close to the actual hypocenter (i.e., nucleation point A), produce a rupture path consistent with observations; other nucleation locations (B through E) either lead to premature rupture arrest or propagation to the M7.1 segment, contrary to observations. These results can be explained by examining the time-dependent stress transfer between the fault segments, as noted below.
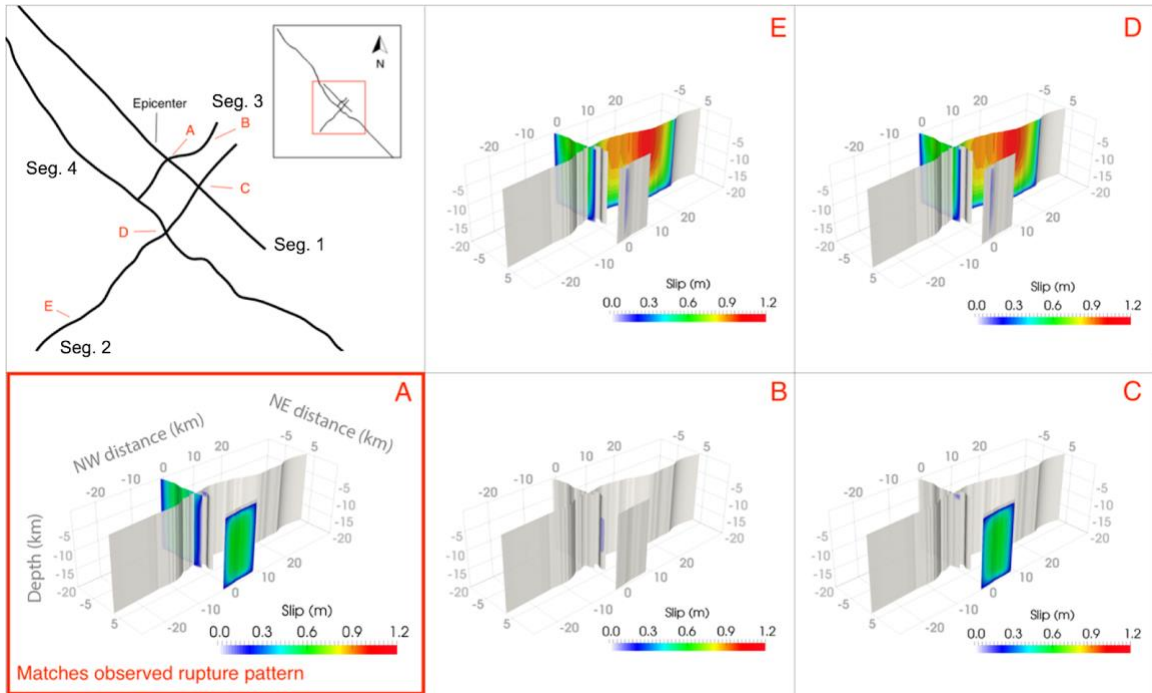
Figure 2.1. Modeled fault geometry in map view and fault slip patterns for different hypocenter locations A through E. The schematic in the top left panel displays 4 non-planar segments for the fault geometry. Only hypocenters on the buried right-lateral segment (including hypocenter A) produce the observed rupture path.

2.3.2 Effect of shear stress and depth of burial of nucleating segment

We find only a narrow range of initial shear stress values that produces the observed rupture path of nucleation on the nucleating right-lateral segment 1 followed by propagation to the main left-lateral segment 2 without also triggering the main M7.1 segment 4. We also find that the right-lateral nucleating segment 1 must have a rather narrow window of burial depth to allow this observed rupture path. The results of our experiments with shear stress level and depth of nucleating right-lateral fault burial are summarized in Figure 2.2. From the left to right panels, initial shear stress varies from 2.1 MPa to 2.5 MPa, and from the top to bottom panels the depth of burial of the nucleating right-lateral fault segment (i.e., the depth up to which the segment is allowed to slip) varies from 0 km (intersecting the free surface, with slip allowed at the free surface) to 1.5 km. We find that the result closest to the observed rupture path is obtained with an initial shear stress of 2.3 MPa and segment 1 buried to a depth of 1.0 km. In general, a lower initial shear stress level produces rupture paths restricted to the nucleating right-lateral segment 1 (Figure 2.2 panels A, D, and G). High initial shear stress tends to produce not just rupture on the main left-lateral segment 2, but also on the northern half of the main M7.1 segment 4 (Figure 2.2 panels F and I).

An examination of the time evolution of rupture in such models indicates that rupture does not propagate continuously from segment 1, around the corner to segment 2, and then around the next corner to segment 4. Rather, in such cases rupture jumps directly from nucleating segment 1 to segment 4, whereupon it continues propagating across the northern portion of this segment.

We also find that only a narrow window of burial depths for segment 1 produces the observed rupture path. Allowing this segment to slip all the way to the earth's surface (in conflict with observations) leads to more slip near the free surface and does not produce propagation to any of the other fault segments (panels A, B, and C). Burial as deep as 1.5 km prevents the rupture propagating to the main left-lateral segment 2 for our 2.1 MPa and 2.3 MPa initial stress models (panels G and H), and results in propagation to both segments 3 and 4 for our 2.5 MPa model (panel I). We note in Figure 2.3 that assuming a gradient in stress to near zero near the free surface does not significantly change these results.
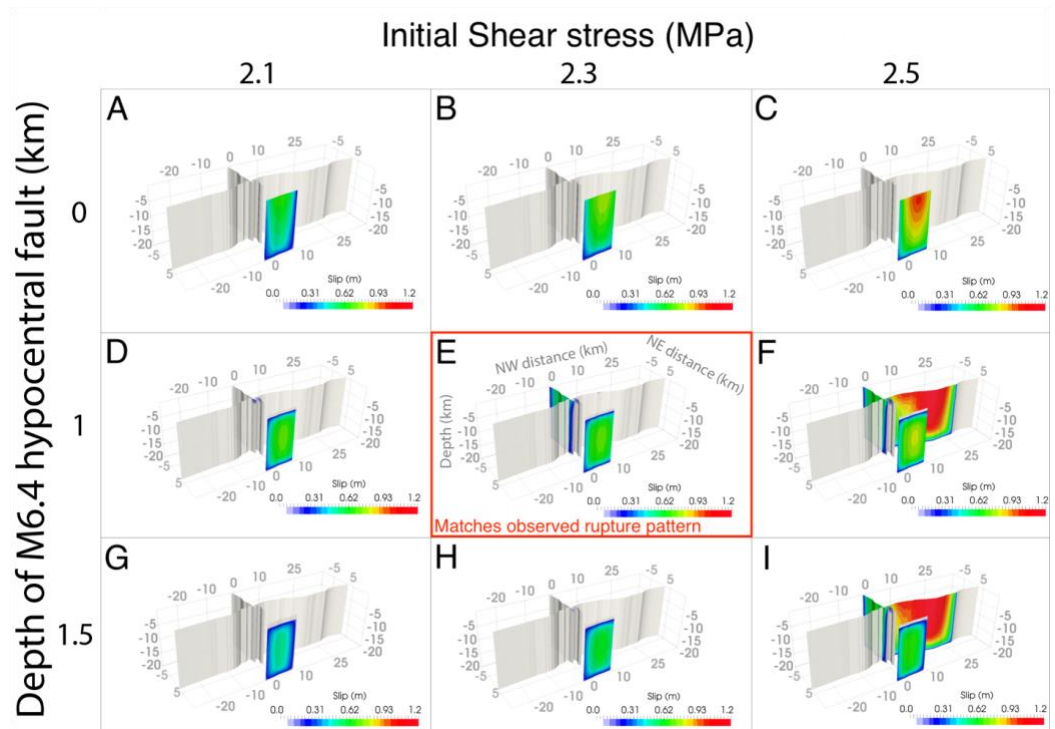
Figure 2.2 Slip on fault system for three different constant initial shear traction levels (2.1 MPa, 2.3 MPa, and 2.5 MPa) and three different depths of burial of the right-lateral nucleating segment (0 km, 1 km, and 1.5 km). The model in the center panel (2.3 MPa shear stress, 1 km depth) is the only model that matches the observed rupture propagation pattern for the M6.4 event.

2.4 Discussion

The results above imply that the observed rupture path of the M6.4 Ridgecrest earthquake was the result of a confluence of multiple factors, including somewhat narrow ranges of shear stress level, the burial depth of the nucleating right-lateral fault segment, and the hypocenter location. Our results are broadly consistent with the dynamic models of Lozos and Harris (2020) and Taufiqurrahman *et al.* (2019) in that these works also indicate that slip on one segment of the fault system can have important effects on the propagation of rupture on nearby segments. In the present work, the simplified setup and exploration of parameter space facilitates in-depth physical interpretations of the complex stress interactions during the earlier M6.4 event.

Figure 2.3 Slip patterns for models in which initial stress tapers from its ambient value at a depth of 1 km to 0.1 times its ambient value at the surface. All models have the nucleating right-lateral segment buried to a depth of 1 km. The preferred model in this parameterization is in the middle panel (red outline), with an initial shear stress level of 2.3 MPa.

Figure 2.4. Slip patterns for models in which initial stress tapers from its ambient value at a depth of 1 km to 0.1 times its ambient value at the surface. All models have the nucleating right-lateral segment buried to a dept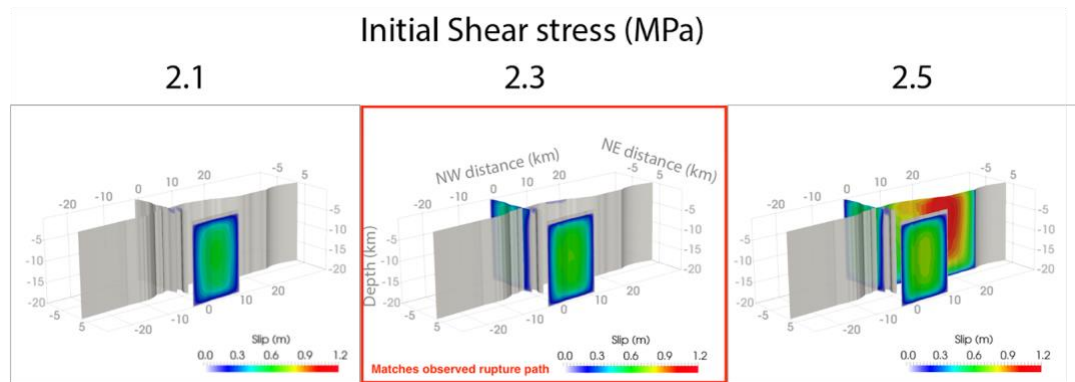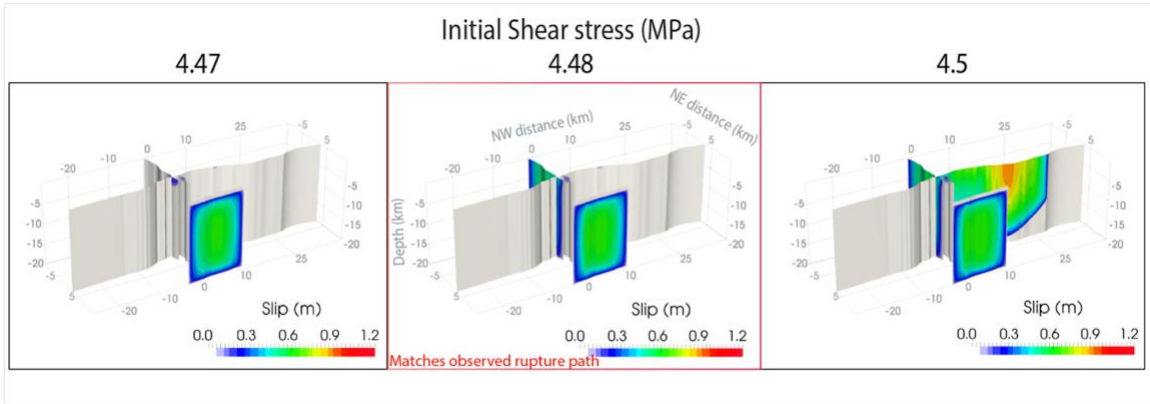h of 1 km. The preferred model in this parameterization is in the middle panel (red outline), with an initial shear stress level of 2.3 MPa.

2.4.1 Hypocenter location

The rupture and slip process on geometrically complex fault systems produces complex time-dependent stress patterns, the details of which can strongly affect the rupture evolution, requiring a form of time-dependent stress analysis (e.g., Oglesby *et al.*, 2008; Kyriakopoulos *et al.*, 2019). The resultant rupture propagation pattern can strongly depend on the order of clamping versus unclamping, and on the effects of directivity—both of which are largely determined by hypocenter location (Oglesby, 2005). Figure 2.4 shows a cartoon of these effects, and the hypocenter locations and corresponding slip patterns are shown in Figure 2.1. For nucleation at the observed hypocenter, slip behind the SE-propagating rupture front on the nucleating segment 1 causes a dynamic unclamping of both segments 3 and 2, which facilitates rupture propagation to both these segments in their SW direction (a dilational bend at their intersections). As explained below, the burial of segment 1 also causes the near-surface portions of segments 2 and 3 to be brought even closer to failure, aiding rupture propagation. A similar effect is seen for nucleation point A (Figure 2.1), which produces a similar rupture path. Further along strike, the rupture due to nucleation at nucleation point C on the buried right-lateral fault, due to its location near the intersections of segments 2 and 3, does not produce enough directivity to induce significant dynamic unclamping of these segments to allow rupture to propagate beyond the very near surface. Nucleation point B produces rupture that dies out shortly after it leaves the forced nucleation zone due to the small size of this segment, which is smaller along strike than the forced nucleation zone.

Rupture from nucleation point E approaches the intersection of segments 2 and 4 from a different direction along segment 2 than the ruptures from the previously-mentioned hypocenters. In this case, rupture propagates a significant distance toward the NE on segment 2, building up stress wave directivity, which amplifies the dynamic unclamping of the NW side of segment 4. For this reason, nucleation at E produces slip across the northern half of the M7.1 earthquake fault. This justification does not fully explain why nucleation at point D produces rupture on both segments 2 and 4, though, given the result that nucleation at the intersection of segments 1 and 2 (hypocenter C) did not produce significant rupture propagation on the intersecting segment. The explanation is found in the observation that the propagation of rupture from segment 2 to segment 4 in this case is not immediate, when the rupture front is in the vicinity of segment 4. Rather, segment 4 takes more than 12 seconds to nucleate and start slipping. In the initial seconds of rupture on segment 2 from hypocenter D, the bilateral rupture produces equal clamping and unclamping from both sides of the intersection, and thus does not facilitate rupture on segment 4. However, as the rupture develops further, there develops an asymmetry in the length of segment 2: there is more area and thus more slip to the SE of the intersection. Thus, after some time has passed, there is an overall unclamping of the NW side of segment 4, which eventually leads to nucleation and propagation of rupture on this segment.

Taken as a whole, we find that only nucleation locations on the buried right-lateral segment 1, a significant distance from the intersection with segment 2, produce rupture propagation patterns consistent with the observed M6.4 earthquake. In particular, nucleation near the SW end of the main left-lateral M6.4 segment 2 would have been much more likely to have triggered at least a large portion of the M7.1 earthquake coseismically, under the assumption that it was equally close to failure as the other segments in the region.

2.4.2 Burial depth of nucleating segment

The depth of burial of the nucleating segment 1 affects the time-dependent stress transfer to neighboring faults, and emphasizes the importance of utilizing more than a simple 2D analysis. Oglesby *et al.* (2003) indicate that when 2 nearby fault segments overlap, slip on one in general will put the other in a stress shadow. However, if the primary segment doesn't overlap completely with the secondary (i.e., in the current case, the secondary segment extends to the surface, while the primary does not), the non-overlapping portion of the secondary is typically brought closer to failure. This mechanism is likely why the Ridgecrest models that propagate to the free surface on segment 1 do not produce any rupture on nearby intersecting faults (panels A, B, and C in Figure 2.2), while models that are buried a small distance can lead to rupture propagation onto the main left-lateral fault segment 2 (panels E, F, and I).

Figure 2.5 illustrates this effect by showing the final (post-event) Coulomb stress transfer from the nucleating right-lateral segment onto the nearby faults in the system. For this figure, slip is allowed only on the right-lateral segment so that its effect on the nearby segments can be more readily assessed. Figure 2.5a shows the results for the buried right-lateral segment (corresponding to the configuration in Figure 2.2E). As expected, slip on the right-lateral fault produces stress shadowing on nearby faults where they overlap with the slipping region at depth. However, there is a strong Coulomb stress increase near the surface on neighboring fault segments near the free surface, at depths where the right-lateral fault does not slip. Due to its closer proximity, the left-lateral M6.4 segment has a stronger Coulomb stress increase than the main M7.1 segment, explaining why in our preferred model the rupture transfers to only the first of these faults. Figure 2.5b shows the results for the surface-rupturing right-lateral fault (corresponding to the configuration in Figure 2.2H), which produces complete stress shadowing up to the surface on nearby faults, hindering rupture propagation.In these models, amplification of stress transfer due to the free surface is also necessary to produce significant stress transfer to the other nearby faults, explaining why models in which the nucleating left-lateral fault is buried 1.5 km below the surface tend not to produce rupture propagation to nearby faults (panels G and H). In Figure 2.2E, the vertical gradient in slip at the top of the right-lateral segment is slightly greater than that of Figure 2.2H, leading to a stronger stress transfer to the main left-lateral fault segment.

Thus, in this parameterization, there is a limited range of fault burial that will produce the combination of effects required to allow the observed rupture propagation. This overall mechanism also helps explain the propagation of rupture to the NE part of the main M7.1 segment 4 in the high (2.5 MPa) initial shear stress models (panels F and I): in these models, rupture does not actually propagate around the fault intersections from the nucleating segment 1 so segment 4; rather, in these models ruptures jump discontinuously from segment 1 directly to segment 4 quite near the surface, in agreement with the idea that the non-overlapping portion of segment 4 is brought closer to failure by slip on segment 1.Lomax (2020) argues that the lack of aftershock activity above approximately 5 km depth on the right-lateral segment 1 implies that the right-lateral fault had little slip above 5 km, in contrast to our relatively shallow preferred model of 1 km burial depth. The Lomax result stands in contrast to the geodetic and seismological models of Li *et al.* (2020) and Pollitz *et al.* (2020), who find quite significant shallow slip of up to 1 m on this segment. Our model is more consistent with the latter results, but we note that the general mechanism in this paper of rupture transfer from the right-lateral to the left-lateral segment via a coulomb stress increase on the shallower part of the left-lateral segment would likely apply in either case.

2.4.3 Shear stress level

In general, a higher initial shear stress makes all the fault segments more favorable for rupture. Low shear stress levels limit rupture to the nucleating segment, whereas the highest shear stress levels facilitate rupture propagation to the M7.1 segment 4 as well as the main M6.4 segment 2. Only for a limited range of initial shear stress levels can the rupture propagate to segment 2 without jumping to segment 4.
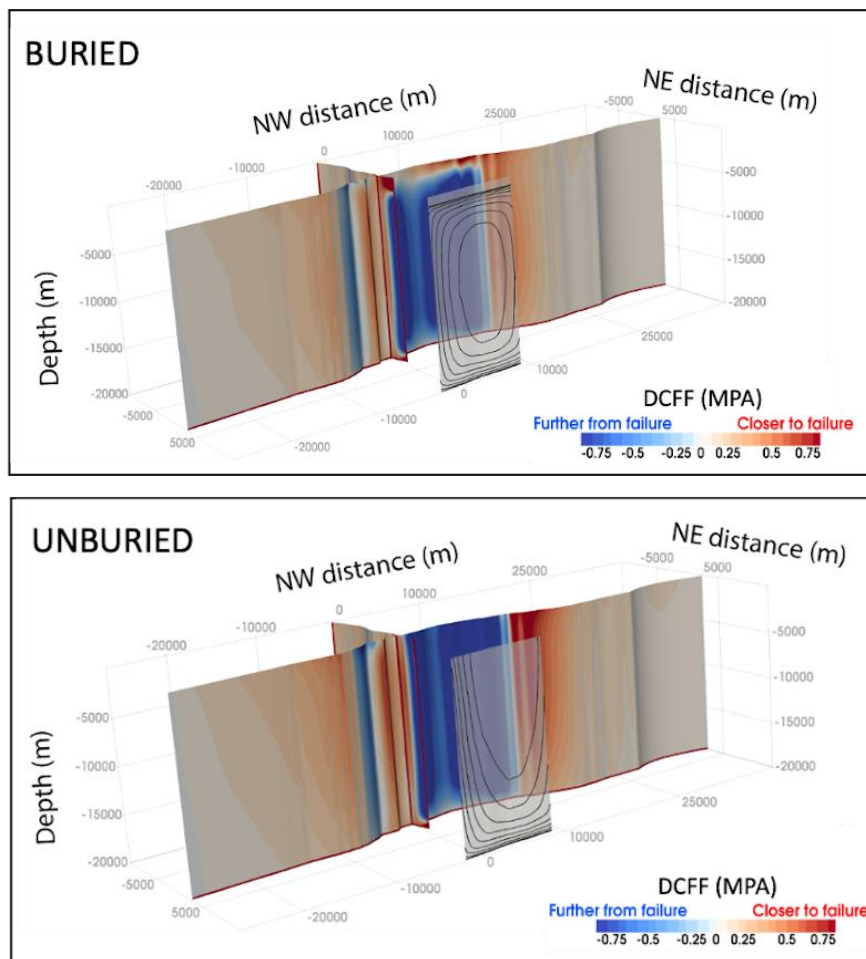
Figure 2.5 Comparison of the change in Coulomb Failure Function between buried (left) and surface-rupturing (right) nucleating right-lateral segment. Burial of the right-lateral segment results in an increase of Coulomb stress near the surface on nearby faults, facilitating rupture to the main M6.4 left-lateral fault segment. Surface rupture on the right-lateral segment results in a decrease in Coulomb stress over the entire depth of the nearby segments, hindering rupture propagation.

2.5 Conclusion

The 2019 M6.4 Ridgecrest earthquake was a complicated event with a complex fault structure and highly heterogeneous rupture propagation and slip (Kendrick *et al.*, 2019; Ross *et al.*, 2019; Li *et al.*, 2020), which in turn were likely strongly affected by heterogeneous stress, frictional properties, rock materials, and other properties. Our simple models are not designed to capture this full complexity; rather, they are designed to investigate the physical origin of the overall rupture path in this earthquake—in particular, the propagation of the rupture from a buried right-lateral fault across a right angle to a left-lateral fault, all without immediately triggering the M7.1 fault that ruptured only 36 hours later. The fact that the present work can explain the rupture propagation pattern via constrained ranges in the overall stress level, the depth of burial of the nucleating segment, and the location of the hypocenter, is compelling evidence that the rupture propagation is explainable without resorting to the fine tuning of a number of not-well-constrained parameters and physical processes. The precise ranges of shear stress level, fault segment burial depth, and hypocenter location determined in this current study should not necessarily be taken quantitatively at face value, as their precise numerical values are surely related to the myriad assumptions required in this (and every) numerical model.

Rather, the conclusion should be that there exist ranges in these parameters that allow the observed rupture path, and that there are relatively straightforward physical explanations behind these ranges. The examination of multiple models that do **not** fit the observations allows a better understanding of the physical processes as well.

The results imply that the rupture path of the M6.4 event was not a foregone conclusion—small changes in a few initial or boundary conditions could have led to very different rupture propagation patterns. This result may hold true for earthquakes in general, rendering the prediction of rupture propagation in future events quite uncertain, and therefore requiring the modeling of many different sets of input parameters to bracket possible faulting behavior. Significantly, the current results depend strongly on the nucleation of the earthquake on a previously-unknown fault segment, whose depth of burial was obviously also unknown. Thus, earthquake models that nucleate only on previously-mapped faults may well underestimate the range of possible faulting behaviors on those previously-mapped faults. To model higher-order observables such as fault slip amplitude and ground motion of course will require even more detailed information, but it still will be helpful to start with simple models, and add complexity gradually as one attempts to model more detail.

References

Andrews, D. J. (1976). Rupture propagation with finite stress in antiplane strain, *Journal of Geophysical Research* 81, 3575-3582.

Barall, M. (2009). A grid-doubling technique for calculating dynamic three-dimensional spontaneous rupture on an earthquake fault, *Geophysical Journal International* 178, 845-859.

DeDontney, N., J. R. Rice, and R. Dmowska (2012). Finite element modeling of branched ruptures including off-fault plasticity, *Bulletin of the Seismological Society of America* 102, 541-562.

Douilly, R., D. D. Oglesby, M. L. Cooke, and J. L. Hatch (2020). Dynamic models of earthquake rupture along branch faults of the eastern San Gorgonio Pass region in California using complex fault structure, *Geosphere* 16, 474-489.

Harris, R. A., M. Barall, D. J. Andrews, B. Duan, S. Ma, E. M. Dunham, A.-A. Gabriel, Y. Kaneko, Y. Kase, B. T. Aagaard et al. (2011). Verifying a computational method for predicting extreme ground motion, *Seismological Research Letters* 82, 638-644.

Harris, R. A., M. Barall, R. J. Archuleta, E. M. Dunham, B. Aagaard, J.-P. Ampuero, H. S. Bhat, V. Cruz-Atienza, L. Dalguer, P. Dawson et al. (2009). The SCEC/USGS dynamic earthquake rupture code verification exercise, *Seismological Research Letters* 80, 119-126.

Kase, Y., and K. Kuge (1998). Numerical simulation of spontaneous rupture processes on two non-coplanar faults: the effect of geometry on fault interaction, *Geophysical Journal International* 135, 911-922.

Kase, Y., and K. Kuge (2001). Rupture propagation beyond fault discontinuities: significance of fault strike and location, *Geophysical Journal International* 147, 330-342.

Kendrick, K. J., S. O. Akciz, S. J. Angster, J.-P. Avouac, J. Bachhuber, S. E. Bennett, K. Blake, S. Bork, B. A. Brooks, P. Burgess et al. (2019). Geologic observations of surface fault rupture associated with the Ridgecrest M6.4 and M7.1 earthquake sequence by the Ridgecrest Rupture Mapping Group, in *2019 SCEC Annual Meeting*, Palm Springs, CA.
Kyriakopoulos, C., D. D. Oglesby, T. K. Rockwell, A. J. Meltzner, M. Barall, J. Fletcher, and D. Tulanowski (2019). Dynamic rupture scenarios in the Brawley Seismic Zone, Salton Trough, Southern California, *Journal of Geophysical Research* 124, 3680-3707.

Li, S., G. Chen, T. Tao, P. He, K. Ding, R. Zou, J. Li, and Q. Wang (2020). The 2019 Mw 6.4 and Mw 7.1 Ridgecrest earthquake sequence in Eastern California: rupture on a conjugate fault structure revealed by GPS and InSAR measurements, *Geophysical Journal International* 221, 1651-1666.

Lozos, J. C., and R. A. Harris (2020). Dynamic Rupture Simulations of the M6.4 and M7.1 July 2019 Ridgecrest, California, Earthquakes, *Geophysical Research Letters* 47, e2019GL086020.

Lomax, A. (2020). Absolute location of 2019 Ridgecrest seismicity reveals a shallow Mw 7.1 hypocenter, migrating and pulsing Mw 7.1 foreshocks, and duplex Mw 6.4 ruptures, *Bulletin of the Seismological Society of America* XX.

Magistrale, H., and S. M. Day (1999). 3D simulations of multi-segment thrust fault rupture, *Geophysical research Letters* 26, 2093-2096.

Meng, L., J.-P. Ampuero, J. Stock, Z. Duputel, Y. Luo, and V. Tsai (2012). Earthquake in a maze: Compressional rupture branching during the 2012 Mw 8.6 Sumatra earthquake, *Science* 337, 724-726.

Shelly, R. David (2020). A high- resolution Seismic catalog for the initial 2019 Ridgecrest Earthquake Sequence: Foreshocks, Aftershocks, and Faulting complexity, Seismological Research Letters 91(4) DOI: 10.1785/0220190309

Taufiqurrahman, T., A.-A. Gabriel, B. Li, S. Aniko Wirp, T. Ulrich, K. H. Palgunadi, A. Verdecchia, S. Carena, and Z. K. Mildon (2019). High-resolution integrated dynamic rupture modeling of the 2019 M6.4 Searles Valley and M7.1 Ridgecrest earthquakes, in *American Geophysical Union Fall Meeting 2019*, San Francisco.

3.1 The M7.1 mainshock

The M7.1 mainshock of the 2019 Ridgecrest sequence reintroduced the 21st century to the presence of large multi segment rupturing earthquakes in California. The mainshock and respective aftershock seismicity were confined to strike-slip faulting, mostly dextral faulting, extending to approximately 46 km in length with a slight dipping component as shown in the focal mechanisms from SCEDC catalog (Hauksson et al 2020). Numerous field observations of peak dextral slip of 4–5+ m are measured near the epicenter, whereas 3–4 m slip extends to the northwest and southeast over a distance of approximately 10 km (Ponti et al., 2020). Researchers have used a number of different techniques and assumptions to model these field observations of the M7.1 mainshock. Duan et al. 2020 utilized geodetic data and a planar segmented faulting model similar to the observed focal mechanism (Hauksson et al 2020) to produce a slip distribution similar to the field observations. Other Geodetic approaches shown in figure 1.3 include optical images and InSAR displacement constraints (Li et al., 2020), kinematic models using high rate GPS measurements (Chen et al. 2020), and a static slip inversion using satellite imagery (Ross et al 2019). Seismic inversions in figures 1.4a and 1.4b using an inverted stress drop from strong ground motions (Pitarka et al 2021), and a finite fault inverse algorithm (Ji et al.,2002) indicate bilateral rupture, agreeing with slip from the geodetic inversions mentioned above and slip measured directly from field observations.

The consensus using these various geodetic and seismological techniques is that there were highly concentrated patches of slip surrounding the M7.1 hypocenter, a bilateral rupture pattern, and patches of high slip near both endpoints of the mainshock fault, despite the ambiguity of parameters within modeling. However, these inversion models are incapable of providing a physical interpretation of the deformation and resulting displacement. Dynamic models can help explain the physical processes involved in rupture propagation, if provided the constraints on source parameters. Ramos et al 2020 illustrates the importance in coupling forward models with inversion models to produce and provide physical explanations of results that match observations using the 2019 Ridgecrest earthquake sequence as a case study. Figure 1.4c illustrates how models that include a dynamic stress transfer produces slightly more slip near the M7.1 hypocenter; However, this comparison is still considered an excellent fit between the kinematic and dynamic approaches. This behavior correlates well with the dynamic model in figure 1.4a that utilized a stress drop derived from strong ground motions. Ramos et al 2020 justifies and provides not only a robust example of modeling the 2019 Ridgecrest earthquake sequence, but also highlights the effectiveness of a dynamic modeling approach.

In this Chapter, we explore the sources or mechanisms responsible for producing the heterogeneous slip pattern inferred during the M7.1 Ridgecrest mainshock. Specifically, we distinguish slip pattern contributions from fault geometry (interaction of the earthquake rupture with itself) and contributions from stress interactions with the prior M6.4 earthquake. Assuming a non-planar fault geometry and neglecting interaction with the prior earthquake demonstrates the strong influence of complex fault geometry to produce complexity within the slip distribution of the mainshock. Bends and stepovers can serve as barriers to rupture (King et al 1985), and they can also produce stress concentrations during an earthquake that also can affect the rupture propagation and consequent slip (Huang et al 2017). Okuwaki and Yagi (2008) demonstrated that discontinuities within a fault system can lead to complex rupture propagation. They showed that some barriers allow through-going propagation, while others cause rupture to terminate. Nielsen and Knopoff (1998) observed compressional features terminating ruptures and the storage of stress at these sites until they themselves break and initiate motion on the smoother, long reaches of the fault. This suggests that the presence of barriers is capable of producing long-term delayed triggering as interseismic strain gradually increases, producing local stress accumulation and eventually resulting in an earthquake. On the other hand, the presence of barriers during the coseismic period organizes the tractions in a pattern that influences both rupture propagation and the slip distribution, which could be responsible for short-term delayed triggering.

Stress shadow barriers can be caused by closely spaced overlapping faults and can be created through both static and dynamic stress transfers to and from nearby faults. Toda et al. (2012) distinguishes the effects of static and dynamic stresses by arguing that spontaneous fault slip causes small static stress changes capable of producing stress shadowing, and coseismic waves cause large dynamic stress changes allowing for triggering over large distances. These authors also observe a decrease in aftershocks due to stress shadowing both from a static and dynamic sense. This chapter focuses on the dynamic effects on rupture propagation caused by stress barriers induced from the fault geometry alone and slip on neighboring faults.

3.2 Method

We use a three- dimensional finite element fault rupture code, FaultMod (Barall 2009), to solve our dynamic earthquake models for the M7.1 mainshock. We determined the mainshock fault geometry (Figure 1.2A) through surface fault traces derived from field mapping (Kendrick et al 2019). We project these mapped surface ruptures vertically 20km into the earth to form our rupture surface. This approach incorporates much of the observed restraining and releasing bends in the fault geometry, allowing for the natural formation of stress heterogeneity due to interactions between different portions of the fault during slip.

Our 4 million hexahedral finite element mesh consisted of two discretization sizes, ~200m near the rupture area, and 600 m in the outer region, to accurately resolve stress and slip on the 46 km long mainshock fault while allowing for computational efficiency. This is essentially the same mesh as in Chapter 2, but with a continuous M7.1 fault at its intersection with the 6.4 left-lateral surface. The main contributors governing earthquake behavior considered in this study are fault geometry and induced traction history. Both source parameters have been determined to dynamically impact the traction conditions and ultimately the overall slip distribution (Harris et al 1993; Oglesby et al 2012; Douilly et al 2020). However, this study's focus is to explore the separate influence each has on the slip distribution of the specific conjugate strike slip fault system corresponding to the Ridgecrest earthquake sequence. We considered two initial traction cases: Constant tractions, and constant tractions plus residual tractions from the M6.4 foreshock (chapter 2) (hereafter denoted the "constant tractions" and "residual tractions" models). The constant tractions for this mainshock model are the same conditions used for our M6.4 foreshock model in chapter 2. For the latter models, we use the static stress pattern left by the final slip in our model of the M6.4 event. Figures 3.1a &3.1b show the heterogeneous slip on the M6.4 fault, which is primarily due to the non-planar characteristics within the fault geometry. This model produced a rupture pattern and average slip similar to that inferred by geodetic and seismic inversion modeling (~1 m maximum) in this early event. The initial shear (figure 3.1c) and normal (figure 3.1d) tractions are set at 2.3 MPa and 6 MPa, respectively.

Our M7.1 residual traction model starts with the same ambient set of tractions as the constant traction model, to which is added the final heterogeneous stress induced by the M6.4's slip. The latter model is likely more realistic because it suggests dependence among neighboring faults and introduces mechanisms such as shear and normal stress shadowing. These two initial stress patterns are compared in figure 3.1, along with our accepted M6.4 slip model. We see that the inclusion of initial stress transfer from the M6.4 foreshock within our M7.1 manifests the consequences of fault interaction by reducing and increasing the shear stress in overlapping and nonoverlapping areas relative to the M6.4 hypocentral fault, respectively. There is a corresponding effect on the normal stress as well, with a different spatial pattern.
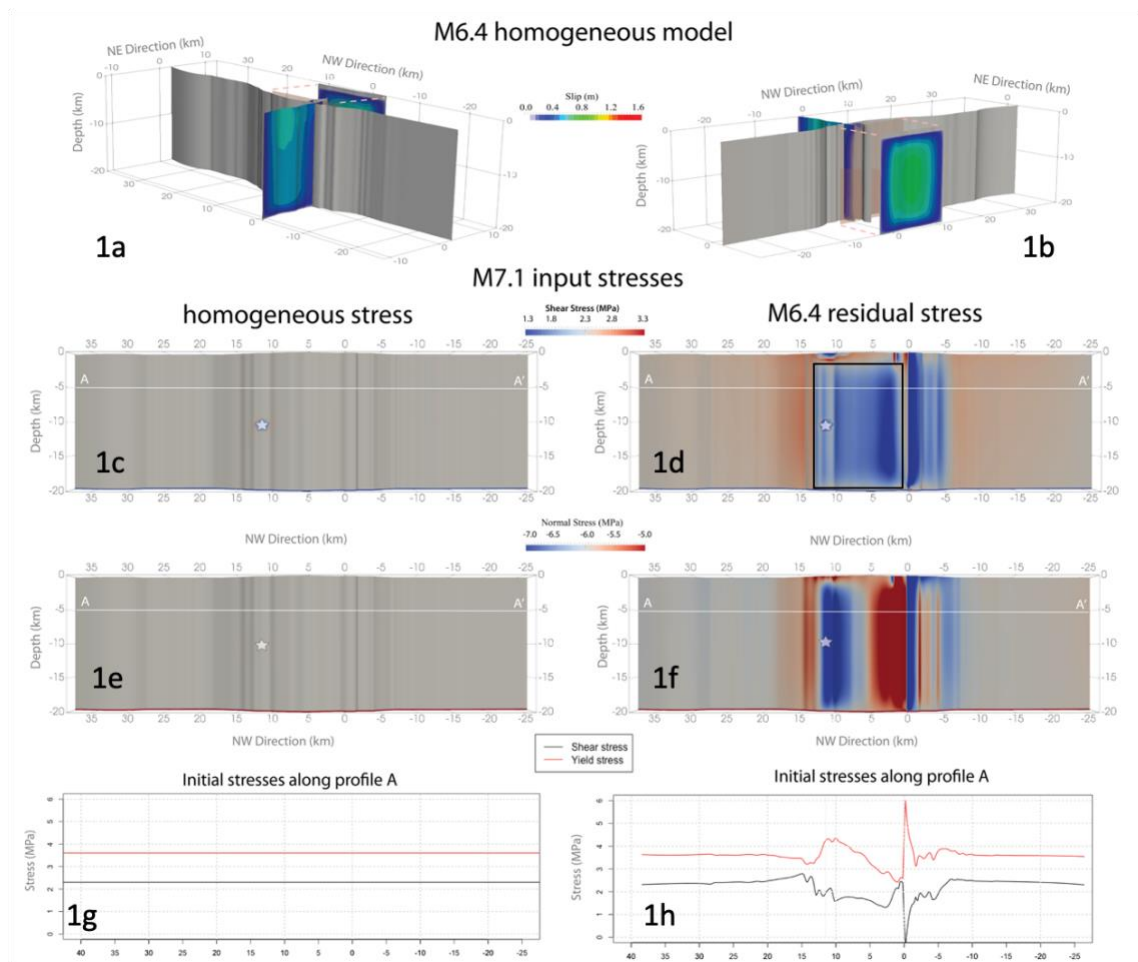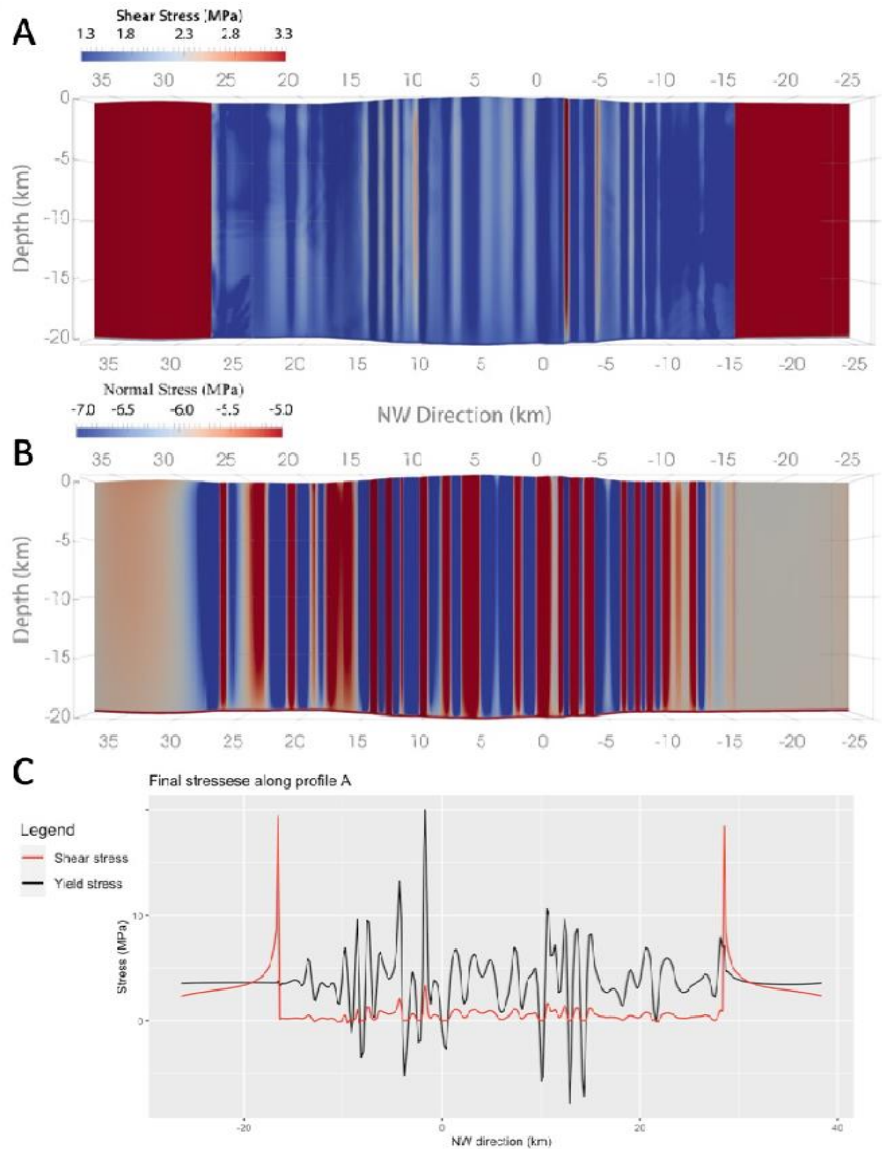
Figures 3.1a & 3.1b Slip from M6.4 model (Cortez et al., 2021) **3.1c & 3.1d** Initial shear and normal stresses for the M7.1 homogeneous model. **3.1e & 3.1f** Initial shear and normal stresses for the M7.1 heterogenous model using residual stress from the M6.4 event. **3.1g & 3.1h** Initial shear and yield (static* n) stress for M7.1 models along profile A.

3.3 RESULTS

3.3.1 Constant traction M7.1 Model

Our preliminary model for the rupture propagation and slip of the 2019 Ridgecrest M7.1

mainshock uses constant traction to isolate and highlight the impact that geometrical

barriers, bends and turns in a strike-slip fault surface can have on the overall slip

distribution. However, the influence of nonplanar surfaces on dynamic rupture causes the

time-dependent and final tractions to become heterogeneous due to restraining and

releasing bends along strike of the mainshock M7.1 fault shown in figures 3.2a and 3.2b.

Note that the final shear and normal tractions have a heterogenous, banded pattern

corresponding to the locations of bends in the fault geometry. This result emphasizes that

the fault's own geometrical complexity has a direct influence on coseismic traction

conditions, and consequently on the slip distribution. In particular, the post-seismic shear

traction increases at geometrical bends along strike near the hypocenter and south of the

intersection (red zones of high shear tractions in figure 2a), while the post-event normal

traction decreases and increases on many alternating bands corresponding to fault bends.

These geometrical bends, or connected stepovers, are considered fault discontinuities

because they introduce stress barriers, thus influencing the nearby background stress. In

general, all stepovers experience an increase in shear stress, while the normal stress is

compressive for restraining stepovers and extensional for releasing stepovers (Wang et al

2020). The normal stresses can become tensile at certain locations of the fault,

corresponding to a complete stress drop.

A stress profile along the fault strike at a depth of 5km provides a visual representation of the traction response to geometrical barriers within the fault geometry prior (figure 3.1c) and post (figure 3.2c) the mainshock. The influence of these bends on the overall slip distribution can be visualized via snapshots of our constant traction model in figure 3.3. The slip distribution at T= 10s shows the beginning stages of the radial rupture propagation, with a slipping region surrounding the hypocenter (figure 3.3a). As time increases to T = 15s (figure 3.3b), the propagation crosses the intersection with the M6.4 event (black dashed line), and approaches a restraining bend (white -dashed line), resulting in a relatively homogenous slip distribution with a few slightly higher slip concentrations. A few time steps later at T = 20s (figure 3.3c), the high slip patches have grown into 2 distinctive high slip concentrations in shallow regions on both sides of the hypocenter north of the intersection, while propagation across the restraining bend produces an interruption of the slip concentration. The bilateral rupture within our slip distribution is consistent with observations of this earthquake (Chen et al 2020;Oral et al 2022). Beyond the restraining bend, another high slip patch forms at T = 25s, while as slip continues, the high slip patches North of the intersection grow and merge as seen in figure 3.3d. Our final slip model in figure 3.3d consists of more concentrated slip south of the M7.1 hypocenter but north of the intersection, and less concentrated slip south of the intersection relative to the geodetic and seismological results as shown in figures 1.3 and 1.4 from chapter 1. Our dynamic models illustrate how high slip concentrations are separated and regulated by restraining and releasing bends in the fault plane.

A

Shear Stress (MPa)

B

Normal Stress (MPa)

NW Direction (km)

C

Final stressese along profile A

Legend
— Shear stress
— Yield stress

Figures 3.2a & 3.2b illustrate the final shear (3.2a) and normal traction (3.2b) along strike the M7.1 mainshock fault. Figure 3.2c provides a line plot comparison of the final shear and yield tractions (Normal*Static coefficient of friction). Notice that the normal tractions go tensile, while the shear tractions approach zero, indicating a complete stress drop.

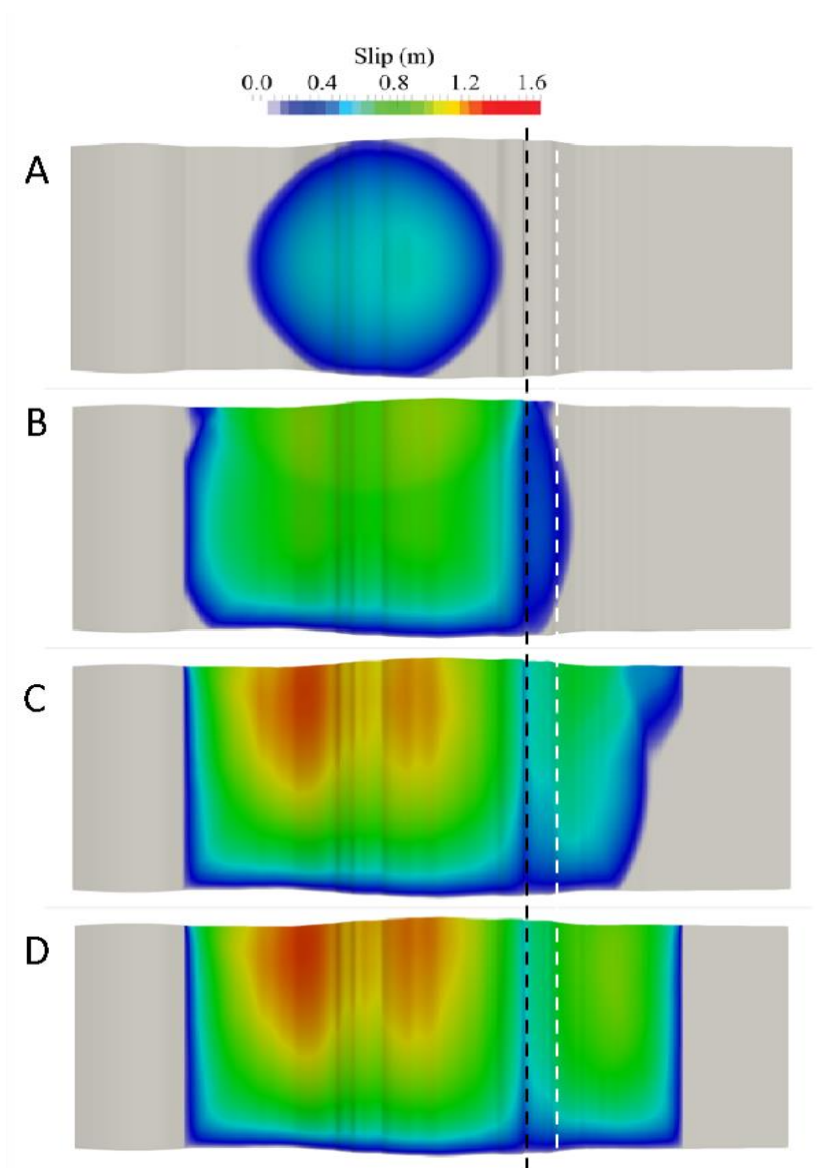Figure 3.3 Displays snapshots of the slip distribution for the constant traction M7.1 model at certain times: 3.3A T=10s, 3.3B T= 15s, 3.3C T =20s, and 3.3D T=25s. The black dashed line outlines the intersection between the M6.4 left lateral and M7.1 mainshock faults, while the white dashed line corresponds to the end of a restraining bend south of the intersection.

3.3.2 M6.4 residual stress M7.1 model

The release of elastic energy from one fault influences the local stress conditions on nearby faults. This concept motivated us to construct a model for the M7.1 mainshock whose initial stress consists of a constant traction model plus the residual stress from our earlier dynamic model of the M6.4 foreshock, as shown in figures 3.1d and 3.1e. Slip on the buried right lateral and surface rupturing left lateral M6.4 faults introduces areas of increased and decreased shear and normal tractions on the M7.1 fault. In particular, the preceding rupture on the buried right lateral M6.4 hypocentral fault causes shear stress shadowing on the nearby parallel mainshock fault between the intersection and 15 km northwest, as shown in figure 3.1d. As mentioned in Chapter 1, the overlapping effect between the two parallel right lateral M6.4 hypocentral and M7.1 mainshock faults is responsible for this shear stress shadowing, but also introduces a shallow zone on the right lateral M7.1 and left lateral M6.4 faults that experiences shear traction increase due to the fact that the right-lateral M6.4 segment does not slip all the way to the free surface. In addition, right lateral strike slip motion on the buried M6.4 segment increases the normal traction on the M7.1 mainshock fault toward the left side of the fault (northwest) and unclamps (decreases) the normal traction on the right side of the fault (near the intersection) shown in figure 3.1F. These effects can be seen more easily in a profile along the strike of the mainshock fault at a depth of 5 km (figure 3.1h).

The initial stress pattern suggests that after the M6.4 earthquake, the fault for the M7.1 mainshock was brought closer to failure near the M7.1 hypocenter location and near the M6.4 left lateral and M7.1 mainshock fault intersection.

The influence of the M7.1 fault geometry on its own residual stress and slip was explored in our constant traction model, but its effects are also apparent in our residual stress models. The final tractions for this M7.1 model using residual stress from the M6.4 earthquake model (figures 3.4a and 3.4b) consists of a similar alternating pattern with respect to its initial value as our constant traction model. Also, a comparison between the shear and normal tractions along profile A for this residual traction model shown in figure 3.4c displays similar results as figure 3.2c. These results show that the restraining and releasing bends in the fault geometry have a significant influence on stress heterogeneity regardless of the initial stress conditions. These cases have shown fault geometry having a stronger dynamic influence on final traction heterogeneity than initial stress conditions (Biemiller et al 2022, Aochi et al 2010; Fukuyama 2015). However, our models demonstrate how traction interaction from foreshock faults influence the rupture propagation, and furthermore the final traction and overall slip distribution, on the mainshock fault.

The influence of the residual stress from the M6.4 earthquake on the M7.1 event is manifested in the slip distribution and visualized using snapshots in figure 3.5. The snapshot at t = 10s in figure 3.5a demonstrates the outset of initial low shear tractions reducing the magnitude of the slip as the rupture propagation enters the strongly shadowed region. Along with the bends in the fault geometry in this region, the low initial shear stress decreases the stress drop and thus the slip in this region. The next snapshot at T=15s emphasizes this discontinuity and relatively low slip as the rupture continues to propagate through the shadowed region. Note that the slip in the top 1 km is not shadowed due to the vertical offset from the buried hypocentral M6.4 fault. The final 2 snapshots display the slip as rupture crosses the low stress drop and bent intersection between the M6.4 and M7.1 faults (figure 3.5c) and approaches a releasing bend south of the intersection. These areas are near releasing bands along the strike of the mainshock fault, which corresponds to high slip concentrations in our final slip distribution (figure 3.5d).
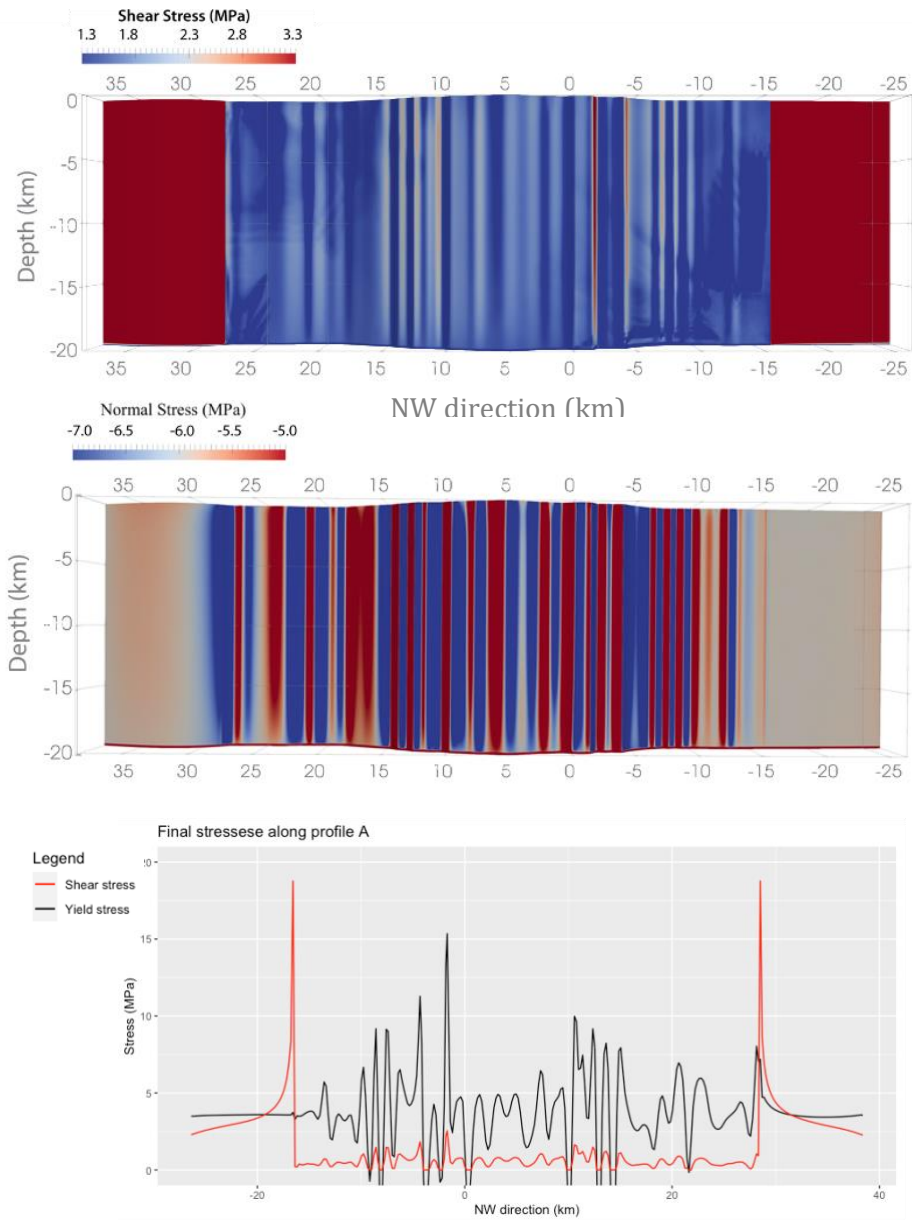
Figures 3.4 Illustrates the shear (3.4a) and normal (3.4b) tractions for the M7.1 residual traction model, while Figure 3.4c compares the shear and yield tractions on a line plot. The yield stress peak just north of the intersection is slightly low compared to Figure 3.2C, suggesting less fault opening because the normal tractions aren't as tensile as the constant traction case due to the shear stress drops to zero.
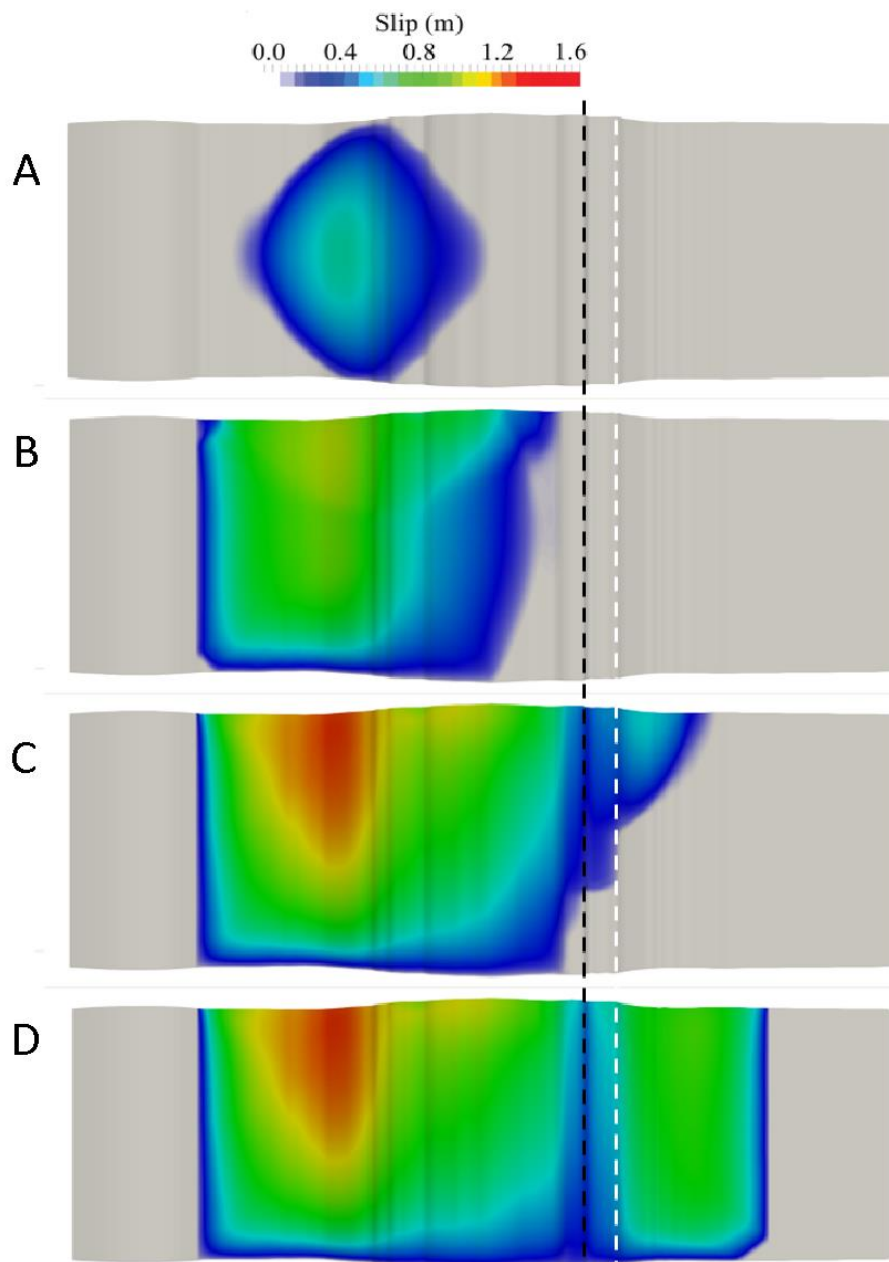
Figures 3.5. Provides a visualization of the resulting slip due to the residual traction model source parameters for: 3.5a T = 10s, 3.5b T= 15s, 3.5c T= 25s, and 3.5d T= 35s. The black dashed line outlines the intersection between the M6.4 left lateral and M7.1 mainshock faults, while the white dashed line corresponds to the end of a restraining bend south of the intersection. Notice that the propagation is slightly slower in this case than the constant traction model in Figure 3.3.

3.4 DISCUSSION- Self- induced and traction interaction influences on slip distribution

3.4.1 The effects of complex geometry

A complex system of fault bends within our fault geometry introduces dynamic stress heterogeneity, suggesting that purely planar faulting models, even those with stress heterogeneity motivated by complex geometry, may not capture important dynamic effects. Pitarka et al. (2021) used a finite difference dynamic modeling approach and planar fault geometry with stress heterogeneity, accounting for nonlinearity along the fault strike by proxy using traction heterogeneity, to model this M7.1 earthquake. These assumptions may introduce artificial effects within a model, namely unrealistically smoothed or overcompensated traction patterns caused by over-parameterization in stress to account for un-modeled geometrical heterogeneity. Our project is designed to avoid these artifacts in describing the influence that non-planar faulting has on rupture propagation and the consequent heterogeneous slip distribution (figure 3.3d). The first snapshot in figure 3.3 underlines how restraining bends can reduce the magnitude of slip and releasing bends can increase slip (figure 3.3b). The presence and effects of these bends within the mainshock fault geometry is visualized by relating the locations of the bends on the M7.1 fault's surface traces from a map's view with final normal tractions for both the constant and residual traction models in figure 3.6.

Right lateral motion within the ensemble of bends and connected stepovers on the M7.1 fault introduces bands of increased and decreased normal tractions. Restraining bend locations near the M7.1 hypocenter and south of the faults' intersection in figure 3.6 correlate with relatively high shear and normal tractions for both the constant traction and residual traction models. On the other hand, releasing bends throughout the fault surface consist of small local stepovers with an overall decrease in shear and normal tractions for both the constant and residual traction models. This analysis suggests that fault complexity has a strong influence on traction interactions, regardless of initial traction conditions. In addition, this comparison highlights the significance these bends have on the final tractions and influence on the overall magnitude of slip. We observed releasing bends leading to high concentrated slip regions in the overall slip distribution as shown in figure 3.3d, while the restraining bends introduce stress barriers, and thus regulate the heterogeneity in slip.
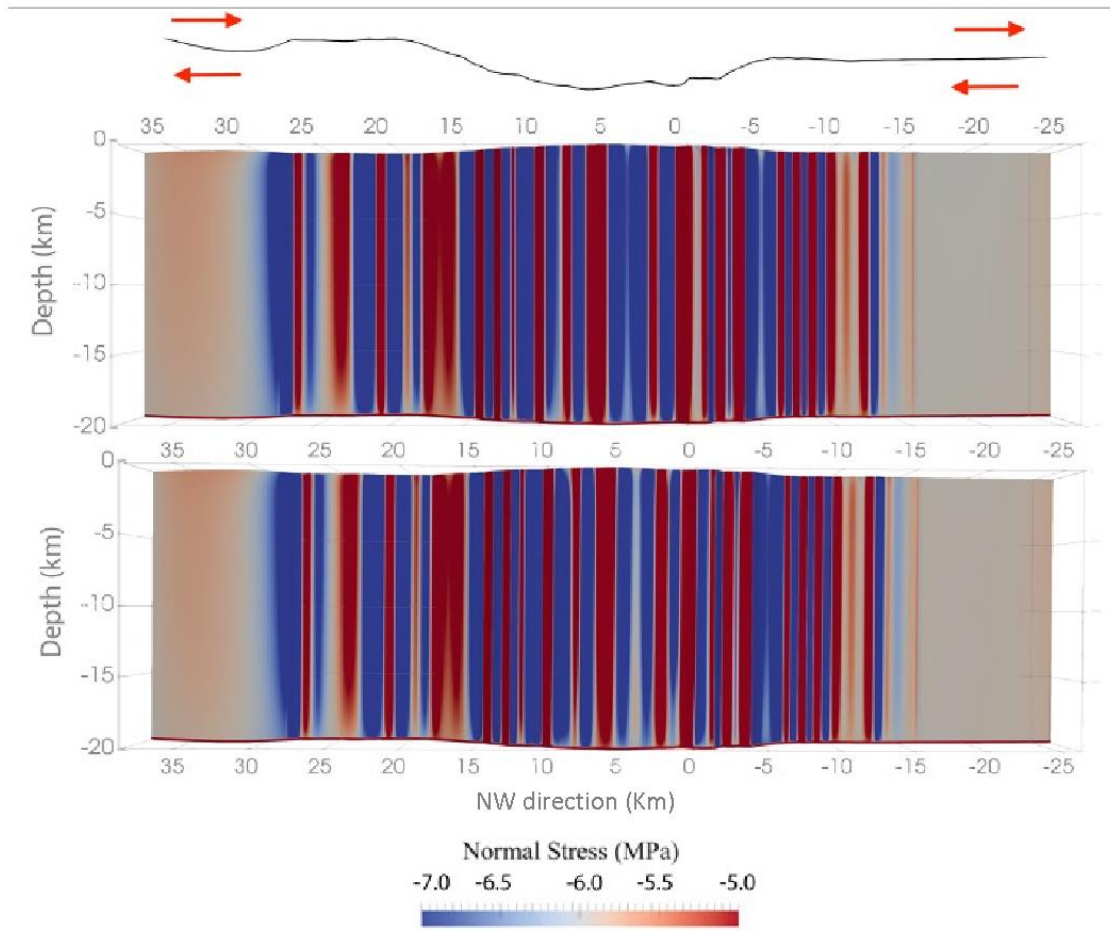
Figure 3.6 A bird's eye view schematic of the M7.1 fault alongside the final Normal tractions for both the constant and residual traction models. Despite different initial traction conditions, the normal final tractions for both models are in strong agreement due to the restraining and releasing bends in the fault geometry.

3.4.2 The effects of shear stress shadowing

Incorporating a priori traction history within our dynamic models establishes a dependence among faults within a fault system, especially neighboring faults. A dynamic model approach provides insight into the physical mechanisms behind the observations from inversion modeling. Our residual dynamic models demonstrate the importance of incorporating nearby fault slip history in refining the initial stress distribution, which underlines mechanisms responsible for governing interactions between faults such as shear stress shadowing. Such shadowing can decrease the shear stress and increase the normal stress, and consequently reduce the slip in that region on a targeted fault due to rupture propagation along a nearby fault (Ghosh et al 1992; Harris 1998). We observed this effect on the M7.1 mainshock fault within the black box in figure 3.1d caused by previous slip from the M6.4 foreshock. This zone consists of significantly low shear tractions because of its orientation and distance from the release of elastic energy from the nearby parallel prior M6.4 event's right lateral fault. Lozos and Harris's (2020) dynamic models of the M7.1 mainshock also emphasize that the self-influence complex geometry leads to heterogeneity in the slip distribution. However, the lack of shear stress shadowing in their model is primarily due to not incorporating the M6.4 right lateral hypocenteral fault. Accounting for both self-induced and neighboring faults' influence on coseismic tractions provides a dynamic model that produces a more realistic slip distribution.

The final stress analysis along profile A for both the constant traction model (figure 3.2c) and residual traction model (figure 3.4c) illustrate this significance dependence in normal traction relative to the change in shear tractions near discontinuities and stress shadowed region within the fault geometry. Overall, both models produce a similar traction pattern due to the strong influence of the mainshock's fault geometry. However, a contrast between the tractions along profile A indicate higher normal tractions within the stress shadowed region and lower shear tractions south of the intersection for the residual model. This final traction pattern produces our accepted slip distribution, which matches better with slip models based on observations. In other words, including the residual tractions from the previous M6.4 foreshock improves the fit between our M7.1 residual traction slip model and observational inverse models (figure 1.4).

3.4.3 Comparison to observationally-determine slip patterns

The inclusion of traction conditions derived from fault interactions (figure 3.5) produces a slip model that agrees more with accepted slip distributions constructed from inversion modeling (figures 1.3 and 1.4) compared to our simpler constant traction model in figure 3.3. Despite the non-uniqueness and variability among inversion models, the consistent observations from the final slip distributions from figures 1.3 and 1.4 are two highly concentrated slip patches with a slightly higher slip path northwest of the M7.1 hypocenter. There are still significant discrepancies among these models such as the overall slip distribution and the total amount of slip. The maximum slip produced by the geodetic inversion models vary depending on the technique with more displacement using InSAR (figs 1.3A and 1.3C) compared to only GPS data (fig 1.3B). The seismic inversion in figure 1.4b produces less slip than the geodetic inversion but agrees slightly better with field displacement measurements. And incorporating an inferred stress drop from strong ground motion within dynamic modeling (figure 1.4a) produces a slip distribution that's qualitatively consistent with the field observations.

3.5 Conclusion

The M7.1 mainshock that occurred on July 6th, during the 2019 Ridgecrest earthquake sequence resulted in ~50km of ruptured fault within a multi-segmented left-stepping right lateral system. The surface ruptures obtained from the field observations in figure 1.2A and seismicity obtained from seismic stations in figure 1.2C suggest that many left stepping connected stepovers at depth form a continuous fault during the release of seismic energy from the M7.1 mainshock and following aftershocks. An interesting observation is the gap (<5 km) between the M7.1 fault and M6.4 buried right lateral hypocentral fault, along with the intersection of the M7.1 fault with the M6.4 left lateral surface rupture. Despite the lack of immediate triggering after the M6.4 foreshock, Geodetic studies suggest re-rupture of an unruptured region on the left lateral M6.4 fault at depth after the M7.1 mainshock, not detected from field observations (Funning et al 2020). This behavior is directly related to the environmental stress within the walker lane and fault interaction from neighboring faults. The fault orientations in this area are conjugated right-lateral faults en echelon to left lateral strike slip faulting known as duplexes and are considered non-sequential 'Riedel' fractures at fault offsets (Woodcock N.H. & Fischer M (1986).

This fault interaction plays an important role in the dynamics of rupture propagation pertaining to its continuation or termination. Studies have demonstrated how dynamic stress perturbations from rupture propagation can lead to ruptures being able to jump stepovers. [e.g., Harris et al., 1991; Harris and Day, 1993; 1999; Lozos et al., 2012; Ryan, 2012].Due to the regional stress in the walker lane, multi-segmented ruptures (rupture jumping over stepovers) are common within the eastern California shear zone/ Southern walker lane. The 1992 Landers and Hector mine earthquakes, located just south of the Walker Lane, exhibited a huge amount of slip distributed amongst multiple left-lateral fault segments. We argue that the mechanisms responsible for these large historical earthquakes, could have been present during the rupture of the M7.1 mainshock. For simplicity, we considered a continuous left lateral fault with many restraining and releasing connected stepovers traced out by the surface ruptures. This approach does assume that the stepovers are connected creating a non-planar fault with self-induced traction capabilities. We demonstrated that the presence of these connected stepovers within the mainshock's fault geometry dynamically influenced the final heterogenous tractions. Our constant traction model for the mainshock exhibits final heterogenous tractions and consequently slip heterogeneity, due to the bends and turns in the fault geometry. The slip distribution in our constant traction model is overestimated because it disregards fault interaction. Namely, previous slip on the neighboring M6.4 fault introduces shear stress shadowing, which reduces the shear tractions in the shadowed region on the mainshock.

However, models that account for the stress transferred from the M6.4 earthquake provide an explanation for some of the low slip areas on the M7.1 fault. Our residual traction model introduces realistic behavior by incorporating the residual tractions from the M6.4 foreshock into the initial conditions. This residual traction case is considered a more robust model because it doesn't neglect fault interactions, thus resulting in a slip distribution with stronger agreement with inverted slip models and direct field observations. In essence, the contrast between our constant traction and residual traction models expresses and identifies the influences responsible for rupture propagation producing the observed heterogeneous slip distribution.

References

Aochi,H; Kato,A (2010). Dynamic rupture of crosscutting faults: A possible rupture process for the 2007 Mw 6.6 Niigata-ken Chuetsu-Oki earthquake. Journal of GeophysicalResearch: Solid Earth. https://doi.org/10.1029/2009JB006556

Biemiller, J; Gabriel, A; Ulrich,T (2022). Dueling dynamics: competition between detachment rupture, splay faults, & off-fault damage. Research Square. https://doi.org/10.21203/rs.3.rs-1650728/v1

Carena, S., and J. Suppe (2002). Three-dimensional imaging of active structures using earthquake aftershocks: The Northridge thrust, California, J. Struct. Geol. 24, 887–904, doi: 10.1016/S0191-8141 (01)00110-9.

Chen, K., Avouac, JP., Aati, S (2020). Cascading and pulse-like ruptures during the 2019 Ridgecrest earthquakes in the Eastern California Shear Zone. https://doi.org/10.1038/s41467-019-13750-w

Cunningham,W. Owen, L. Snee, L. Li, Jiliang (2003). Structural framework of a major intracontinental orogenic termination zone: the easternmost Tien Shan, China. Journal of the Geological Society, London, 160, 575–590.

Cunningham, W.D and Mann, P; Tectonics of strike-slip restraining and releasing bends (2007). Geological Society, London, Special Publications, https://doi.org/10.1144/SP290.1

Douilly,R. Oglesby, D. Cooke,M. Hatch,J (2020). Dynamic models of earthquake rupture along branch faults of the eastern San Gorgonio Pass region in California using complex fault structure. Geosphere 2020; 16 (2): 474–489. doi: https://doi.org/10.1130/GES02192.1

Duan, H, Chu,Z , Zhang,S , Yang,C, Chen,J , Lei,J. 2022. Analysis of coseismic slip distributions and stress variations of the 2019 Mw 6.4 and 7.1 earthquakes in Ridgecrest, California, Tectonophysics, Volume 831,https://doi.org/10.1016/j.tecto.2022.229343.

Fukuyama,Eiichi (2015). Dynamic faulting on a conjugate fault system detected by near-fault tilt measurements. Earth, Planets and Space 67:38 DOI 10.1186/s40623-015-0207-1

Funning,G. Floyd,M. Terry, R (2020). Distinguishing slip from the M6.4 and M7.1 Ridgecrest earthquakes using campaign GPS and InSAR data . Earth and Space Science Open Archive doi: 10.1002/essoar.10501396.1

Ghosh, U., A. Mukhopadhyay, and S. Sen (1992). On two interacting creeping vertical surface-breaking strike-slip faults in a two-layer model of the lithosphere, Phys. Earth Planet. Inter., 70, 119-129.

Harris,R. Day,S (1993). Dynamics of Fault Interaction: Parallel Strike-Slip Faults. Journal of Geophysical Research, VOL. 98, NO. B3, PAGES . U.S. Geological Survey, Menlo Park, California. 4461-4472,
Harris, R. A. (1998), Introduction to Special Section: Stress Triggers, Stress Shadows, and Implications for Seismic Hazard, J. Geophys. Res., 103(B10), 24347– 24358, doi:10.1029/98JB01576.

Hauksson, E., C. Yoon, E. Yu, J. R. Andrews, M. Alvarez, R. Bhadha, and V. Thomas (2019). Caltech/USGS Southern California Seismic Network (SCSN) and Southern California Earthquake Data Center (SCEDC): Data Availability for the 2019 Ridgecrest Sequence, Seismol. Res. Lett. 91 (4), 1961–1970, doi: 10.1785/0220190290

Huang, Y. Ellsworth,W. and Beroza,G (2017).Stress drops of induced and tectonic earthquakes in the central United States are indistinguishable. Science Advances, vol 3 number 8.DOI: 10.1126/sciadv.1700772

Hui Wang, Mian Liu, Benchun Duan, Jianling Cao; Rupture Propagation along Stepovers of Strike-Slip Faults: Effects of Initial Stress and Fault Geometry. Bulletin of the Seismological Society of America 2020;; 110 (3): 1011–1024. doi: https://doi.org/10.1785/0120190233

Jolivet,L. Tamaki, K. Fournier,M (1994). Japan Sea, opening history and mechanism: a synthesis. Journal of Geophysical Research, 99, 22 237–22 260.

King, G., & Nábělek, J. (1985). Role of Fault Bends in the Initiation and Termination of Earthquake Rupture. Science, 228(4702), 984–987. http://www.jstor.org/stable/1694250

 Lozos,J and Harris, R . Dynamic rupture simulations of the M6.4 and M7.1 July 2019 Ridgecrest,California Earthquakes (2020). https://doi.org/10.1029/2019GL086020

Mazzoni, S., Kashida, T., Wang, P., Ahdi, S. K., Bozorgnia, Y., & Stewart, J. P. (2019, 08). Strong Ground Motions from 2019 Ridgecrest Earthquake Sequence Mainshocks. Poster Presentation at 2019 SCEC Annual Meeting.

Nielsen,S. Knopoff,L (1998). The equivalent strength of geometrical barriers to earthquakes. Journal of Geophysical Research Atmospheres DOI: 10.1029/97JB03293

Okuwaki,R. Yagi,Y (2018). Role of geometric barriers in irregular-rupture evolution during the 2008 Wenchuan earthquake, Geophysical Journal International, Volume 212, Issue 3, March 2018, Pages 1657–1664, https://doi.org/10.1093/gji/ggx502

Parker, G, Baltay, A, Rekoske,J, THompson,E (2020). Repeatable Source, Path, and Site Effects from the 2019 M 7.1 Ridgecrest Earthquake Sequence. Bulletin of the Seismological Society of America 110(4), DOI 10.1785/0120200008

Oglesby,D. Martin, P (2012). Fault geometry, rupture dynamics and ground motion from potential earthquakes on the North Anatolian Fault under the Sea of Marmara, Geophysical Journal International, Volume 188, Issue 3, March 2012, Pages 1071–1087, https://doi.org/10.1111/j.1365-246X.2011.05289.x

Oral, E., Ampuero, J., & Asimaki, D. (2022, 09). The role of sediments and fault damage on the 2019 Ridgecrest earthquake: a rupture impediment and/or ground motion amplifier?. Poster Presentation at 2022 SCEC Annual Meeting.

Ponti, D.J., Blair, J.L., Rosa, C.M., Thomas, K., Pickering, A.J., Dawson, T., Akciz, S., Angster, S., Bacon, S., Barth, N., Bennett, S., Blake, K., Bork, S., Bormann, J., Brooks, B., Bullard, T., Burgess, P., DeFrisco, M., Delano, J., Dolan, J., DuRoss, C., Ericksen, T., Frost, E., Funning, G., Gold, R., Graehl, N., Gutierrez, C., Haddon, E., Hatem, A., Hernandez, J., Hitchcock, C., Holland, P., Hudnut, K., Kendrick, K., Koehler, R., Kozaci, O., Ladinsky, T., Madugo, C., Mareschal, M., McPhillips, D., Milliner, C., Morelan, A., Nevitt, J., Olson, B., O'Neal, M., Padilla, S., Patton, J., Philibosian, B., Pierce, I., Sandwell, D., Scharer, K., Seitz, G., Singleton, D., Spangler, E., Swanson, B., Jobe, J.T. , Treiman, J., Valencia, F., Williams, A., Zachariasen, J., and Zinmke, R., (2020). Field observations with quantitative displacement measurements obtained From surfaces faulting and ground deformation features produced by the Ridgecrest M6.4 and M7.1 earthquake sequence of July 4 and 5, 2019: Provisional release 1, in Ponti, D.J., Blair, J.L., Rosa, C.M., Thomas, K., Pickering, A.J., Dawson, T. E., compilers, 2020, Digital datasets documenting surface fault rupture and ground deformation features produced by the Ridgecrest M6.4 and M7.1 earthquake sequence of July 4 and 5, 2019: U.S. Geological Survey data release, https://doi.org/10.5066/P9BZ5IJ9

Ramos, M. D., Neo, J. C., Thakur, P., Huang, Y., & Wei, S. (2020). Stress changes on the Garlock fault during and after the 2019 Ridgecrest earthquake sequence. Bulletin of the Seismological Society of America, 110(4), 1752–1764. https://doi.org/10.1785/0120200027

Toda, S., Stein, R., Beroza, G (2012). Aftershocks halted by static stress shadows. Nature Geosci 5, 410–413. https://doi.org/10.1038/ngeo1465

Woodcock N.H. & Fischer M (1986). Strike-slip duplexes. Journal of Structural Geology 8 (7), 725- 735.

4. Summary

The 2019 Ridgecrest earthquake sequence alarmed California's population, geologists, and seismologists with a seismic case study consisting of large earthquakes (M>6). This case study, located in the southern Walker Lane, exhibited conjugate orthogonal faulting, 2 large earthquakes (M6.4 and M7.1) within 48 hours of each other, and several stepovers connected at depth (Figure 1.2A). Despite the proximity of the conjugate M6.4 right lateral hypocentral fault and left lateral surface trace, the M7.1 didn't immediately rupture in the earlier event. In fact, the elastic energy didn't release until 6 hours after a M5.4 foreshock partially jumped and stressed the M7.1 hypocentral region, which occurred 30 hours post the M6.4 foreshock. The RES produced seismic radiation that traversed the Garlock fault and San Bernardino Mountain range, traveling well into Southern California. These observations were accumulated using direct measurements from field expeditions (Kendrick et al 2019), ground displacements obtained from geodetic approaches (Funning et al 2020; Ross et al 2019), and strong ground motion derived from seismic stations (Rekoske et al 2020).

The complex faulting, seismic radiation, rupture path, and time delay between the large earthquakes during the RES may be related to the tectonic setting within this region of the Walker Lane. The Walker Lane is a geological trough wedged between the Sierra Nevada Mountain range in California and Nevada's Basin. The northern, central, and southern walker lane accommodates 20% of the strain from tectonic motion between the Pacific and Northern American plates.

This tectonic setting of this region is responsible for the orientation of sinistral and dextral fault combinations that intersect well beyond the surface. This complex fault geometry was shown to influence rupture propagation during the 2019 Ridgecrest earthquake sequence. Similarly, the 2016 Nine-mile earthquake sequence exhibited conjugate orthogonal faulting due to three M5 earthquakes and preceding aftershocks in the Northern part of walker lane. However, south of the Garlock fault within the Eastern California shear zone, multisegmented dextral faulting without the orthogonal aspect was observed after the 1992 Landers and 1994 Hector mine earthquake sequences. This suggests that the type of faulting within the walker lane is unique to this section of the zone. Another unique observation of this sequence is the low seismic moment to slip ratio in comparison to the earthquake sequences mentioned within the Northern Walker Lane and Eastern California Shear zone.

Our models of the 2019 Ridgecrest earthquake sequence gradually increased complexity by including more robust source parameters, and in turn each resulted in more agreement to the observed slip distribution and rupture path than our previous simple models. Combining this forward modeling approach on a finite element mesh with flexible fault geometry allows us to include the complexity in fault geometry and interpret its influences on rupture propagation, and consequently slip distribution. The physical mechanisms that our models identify can complement the inversion models in figure.

The inverse approach relies on measurables gathered by various geodetic and seismic apparatuses, where the resolution and methodology are a direct result of the ambiguity across the models. In addition, the time delay between these two events provided the opportunity to place more instruments before the mainshock, allowing for more quantitative observations for the mainshock as opposed to the foreshock. This justifies some of the ambiguity amongst models when deciphering the influence each large earthquake has in the entire earthquake sequence. Despite the ambiguity, the consensus among the types of modeling suggests that the M6.4 primarily ruptured a pair of conjugated dextral and sinistral faults, while the M7.1 resulted in left stepping dextral faulting with 2 high patches of slip on either side of the hypocenter, indicating bilateral rupture. Our forward model approach produced results broadly similar to inverted models for both the M6.4 foreshock and M7.1 mainshock during the RES. We achieved our foreshock model by including a buried hypocentral fault and deriving tractions from an empirical value using the maximum slip measurement, which in turn, introduces areas of minimal stress shadowing, resulting in a conjugate rupture pattern. Our accepted M7.1 mainshock model utilizes the residual stress from our M6.4 foreshock model and geometrical self-induced dynamic tractions to produce a heterogenous slip distribution in strong agreement to field observations and inversion slip models.

In this study we observed a vertical offset in the M6.4 fault geometry that induced tractions governing rupture propagation along with significant differences in the slip between regions near releasing and restraining bends on the M7.1 fault. The M6.4 foreshock rupture propagated from a buried right lateral strike slip fault to a conjugated left lateral surface rupture due to the lack of shear stress shadowing. Regarding the M7.1 mainshock, areas along strike with an increase in both shear and normal tractions correspond to low slip, while regions with a decrease in both shear and normal tractions correspond to high slip. This observation hints at the idea that mechanisms near releasing bends create higher stress drops relative to restraining bends. Understanding how, where and when increases or reductions in tractions occur along a fault is crucial to identify the characteristics of previous or future earthquakes. Utilizing forward dynamic modeling with source parameters using inversion constraints provides models with both parameters from observed data and physical interpretations of their effects. Adopting this approach for earthquake modeling serves as an attempt for an optimal joint inversion model, and has the potential to assess seismic hazards and mitigate risks.

The simplistic approach in this numerical modeling workflow does neglect a few important observations and features. Despite our attempt to constrain the fault geometry completely, we assumed a pure vertical strike-slip fault network by neglecting the slight dipping angle (vertical displacement) that was observed in direct field measurements and focal mechanisms obtained by seismic data. In doing so, the dynamics in our models correspond to more of an artificial effect rather than the realistic physics experienced during the 2019 RES. Nonetheless, our models still address concepts related to conjugated faulting that was observed during this sequence. The inclusion of three-dimensional fault geometry introduces stress heterogeneity that would otherwise need to be accounted for with a user defined stress drop. Also, to avoid a large artificial stress drop we defined a relatively low slip weakening distance of 0.12m to produce a reasonable slip distribution on the small M6.4 hypocentral fault. A feature observed for this earthquake sequence was orthogonal conjugated faulting, which is contradictory to the expected 60 or 120 degrees between faulting under a regional maximum compressive stress according to the Mohr failure criteria and Anderson mechanics. We didn't investigate the physical mechanisms behind this observation but rather used the orthogonal surfaces traces to constrain our fault geometry. Another feature not thoroughly explored in this study was the bilateral rupture and ground motion observed during this sequence.

Because we optimized our models by merely the magnitude of the slip and distribution, and not the temporal evolution of displacement, our models aren't capable of fitting models to those from inverse approaches without incorporating the sources responsible for observed ground response to this energy release during this earthquake sequence. Regardless of these exclusions in our models, this study emphasizes not only the importance in constraining and utilizing as many parameters within modeling, but also addresses how even a simple forward model approach can gain insight on the physical mechanisms that govern earthquake rupture propagation.

References

Funning,G. Floyd,M. Terry, R (2020). Distinguishing slip from the M6.4 and M7.1 Ridgecrest earthquakes using campaign GPS and InSAR data . Earth and Space Science Open Archive doi: 10.1002/essoar.10501396.1

Kendrick, K. J., S. O. Akciz, S. J. Angster, J.-P. Avouac, J. Bachhuber, S. E. Bennett, K. Blake, S. Bork, B. A. Brooks, P. Burgess et al. (2019). Geologic observations of surface fault rupture associated with the Ridgecrest M6.4 and M7.1 earthquake sequence by the Ridgecrest Rupture Mapping Group, in *2019 SCEC Annual Meeting*, Palm Springs, CA

Rekoske, J., E. M. Thompson, M. P. Moschetti, M. Hearne, B. T. Aagaard, and G. A. Parker (2020). The 2019 Ridgecrest, California, Earthquake Sequence Ground Motions: Processed Records and Derived Intensity Metrics, Seismological Research Letters. 91 (4): 2010–2023. doi: https://doi.org/10.1785/0220190292

Ross, Z. E., B. Idini, Z. Jia, O. L. Stephenson, M. Zhong, X. Wang, Z. Zhan, M. Simons, E. Fielding, S.-H. Yun et al. (2019). Hierarchical interlocked orthogonal faulting in the 2019 Ridgecrest earthquake sequence, *Science* **366,** 346-351.